Manuscript # acp-2017-303

Responses to Reviewer #1

This study quantifies global source-receptor relationships of concentration, direct and indirect radiative forcing of sulfate aerosols utilizing an online chemistry-climate model but nudging it with reanalysis winds. They found that sulfate concentrations are mainly local origin in polluted regions, and their concentration efficiencies in terms of unit precursor emissions are high over arid regions with weak export. In addition, they found the indirect radiative forcing of sulfate aerosols is much larger than the direct radiative forcing. I found topic of this paper is interesting and is suitable for publication in this journal. However, substantial improvements are needed before publication. Following are the major and specific issues:

We thank the referee for all the insightful comments to the manuscript and helpful suggestions for improving the presentation quality. Below, we explain how the comments and suggestions are addressed (our point-by-point responses in blue) and make note of the changes that have been made to the manuscript, attempting to take into account all the comments raised here.

Major issues:

1.The authors should articulate the novelty or advance in science or methodology of this study when comparing to previous works. In the introduction, the authors listed a number of similar studies. However, the authors did not describe clearly their motivations to repeat this kind of work as well as the uniqueness of their findings.
Response:

In previous studies about source attribution of sulfate, only a limited number of anthropogenic source regions over the Northern Hemisphere were considered and examined (Park et al., 2004; Heald et al., 2006; Chin et al., 2007; Hadley et al., 2007; Yu et al., 2013; Bellouin et al., 2016; Stjern et al., 2016). Continents and subcontinents over the tropics and Southern Hemisphere are also important source and receptor regions for the sulfate radiative forcing, especially indirect forcing due to stronger aerosol-cloud interactions in clean environments (Koren et al., 2014). Although Liu and Mauzerall (2007) and Liu et al. (2008, 2009) included ten anthropogenic source regions, they only focused on source attribution of sulfate mass concentration without examining sulfate radiative forcing. In addition, few studies have quantified the global source-receptor relationships of sulfate indirect radiative forcing that can be attributed to local/non-local source regions and anthropogenic/natural source sectors.

Certainly, this study is not a repeat of previous work on source-receptor relationships. This is the first study that examines source attribution of sulfate radiative forcing with tagged anthropogenic and natural sources covering the whole globe. In this study, we quantify sixteen source region/sector contributions (fourteen major source regions and two natural source sectors) to regional and global sulfate mass concentrations, and direct and indirect radiative forcing of sulfate. Another novel aspect of this study is that we are using the new emissions datasets generated for the CMIP6 activities. Thus our model configuration and results could potentially be more comparable to future modeling results coming out of the CMIP6 activities than most of the previous studies.

We have revised the introduction section to show these novelties and discussed the differences between our study and previous studies. Please see responses to the more specific comments below.

2.It is unnecessary to discuss the source-receptor relationships in detail since previous works have already reported similar results. These discussions are lengthy and should be shortened substantially (i.e., abstract, sections 4 and 5). Some figures and discussions could be put into the supporting information.

Response:

We have significantly shortened the details of source-receptor relationships in the abstract as suggested. We would like to stress that our systematical analysis is from a variety of angles to describe source-receptor relationships of sulfate concentrations and radiative forcing, including both the near surface concentration and column burden, both direct and indirect radiative forcing, both oceanic and continental regions, both Northern and Southern Hemisphere, both anthropogenic and natural sources, and both absolute and relative contributions. For all these aspects, we don't see overall similar results to previous studies, especially, in a quantitative way. However, we do value the comment on our lengthy discussions, and have tried our best to shorten the source-receptor descriptions in sections 4 and 5.

3.For the method section, the authors may divide it into several subsections (e.g., model description, tracer tagging, model configurations, . . .). In addition, the parameterizations of calculating the DRF and IRF of sulfate need to be described in detail. The method used to calculate the DRF of sulfate from the tagged regions/sectors is also unclear.

Response:

We have now divided it into the suggested subsections: model description, sulfur source-tagging, emissions, and model configurations. We also clarified on the configurations of the list of simulations performed in this study.

We have also revised the description of parameterizations and the approach of calculating DRF and IRF to include more details, as the following:

"Sulfate is internally mixed with other species in the same aerosol mode and then externally mixed between modes. Sulfate refractive indices at visible wavelengths is 1.43+0.00i. Activation of cloud droplets uses the scheme from Abdul-Razzak and Ghan (2000). The model simulates aerosol-cloud interactions in stratiform clouds using a physically based two-moment parameterization (Morrison and Gettelman, 2008). In addition to the standard radiative fluxes calculated in the model by taking into account all aerosols, the CESM has the capability of diagnosing radiative fluxes in parallel for a subset of aerosol species. The difference between the standard and the diagnosed radiative fluxes can then be attributed to the difference in aerosols considered in the radiation calculations. For example, the difference in shortwave radiation fluxes at the top of the atmosphere (TOA) represents the DRF of the excluded aerosol components in the diagnostic calculation (Ghan, 2013). Using this same method, the DRF of sulfate from any of the sixteen individual tagged regions/sectors can be derived from a pair of diagnostic radiation calculations with and without the particular tagged sulfate considered. To estimate IRF of sulfate from different sources, we define in this study an incremental IRF, calculated as $\Delta(F_{clean} - F_{clear,clean})$, where F is the radiative flux at TOA, F_{clean} is the flux calculated neglecting scattering and absorption by aerosols, $F_{clear,clean}$ is the flux calculated neglecting scattering and absorption by both clouds and aerosols, and Δ refers to the differences between the base and emission perturbed simulations."

4.An incremental IRF is defined in this study to quantify the indirect radiative forcing of sulfate. However, there is no validation about this calculation. As the authors mentioned, anthropogenic sources contributed substantially to the incremental IRF over oceans, but few measurements over remote oceans were used to validate their sulfate calculation. The authors may use some aircraft measurements to verify their results over those remote regions.

Response:

The sulfate indirect effect has been fully validated in McCoy et al. (2017) with the same model (CAM5.1-MAM3-PNNL in their study). McCoy et al. (2017) reported that the CAM5.1-MAM3-PNNL model did quite well at producing a reasonable sensitivity of cloud to sulfate mass concentration compared to MODIS satellite data. In addition, in another multi-model intercomparison study including the base simulation results from this work, Fanourgakis et al. (in preparation) evaluates aerosol, CCN and cloud sensitivity in global models against several observational datasets. The incremental IRF in this study is also derived based on the sensitivity of cloud forcing to sulfate (20% of sulfate precursor emission). We have now cited these studies in the revised manuscript instead of duplicating the work.

5.In the introduction, the authors have mentioned that numerous previous studies have examined the sulfate radiative forcing from different sources and regions. However, in the discussion section, they did not carefully compare their results to

previous works. I would suggest the authors pay more attention to the difference between this study and previous works.

Response:

Because we are using different emission datasets and source regions from those in previous studies, a quantitative comparison of source attributions is not so meaningful. However, it is more interesting to compare the radiative forcing efficiency with previous studies. We have now added the Table S9 (see below) to show the comparisons and discussed it at the last section of the manuscript, as the following:

"Table S9 compares the annual sulfate radiative forcing efficiencies simulated in this study to those in previous multi-model studies (Yu et al., 2013; Bellouin et al., 2016; Stjern et al., 2016). As in the previous studies, the DRF efficiency is calculated as the response of global DRF to a 20% reduction in local emissions divided by the 20% of sulfur emissions based on two separate simulations rather than 100% of local emissions in a single simulation (Table S6). The efficiencies based on the 20% emission reduction are very similar to those of the 100% emission reduction, indicating a nearly linear relationship between sulfate DRF and emissions. Compared to Yu et al. (2013) and Stjern et al. (2016), the DRF efficiencies in this study are around the lower bound for all source regions. Another multi-model intercomparison study also reported a lower sulfate DRF simulated in CAM5 compared to other models (Myhre et al., 2013). The difference in DRF efficiencies likely arises from differences in the estimates of aerosol optical properties. With aerosol-cloud interactions included, the total radiative forcing efficiencies in this study are similar to the best estimates provided by Bellouin et al. (2016). The global IRF in CAM5 was also found to be larger than other models in a nine-model intercomparison study, which was attributed to an strong aerosol induced cloud scattering (Zelinka et al., 2014)."

Table S9. Comparison of annual sulfate radiative forcing efficiency (mW m^{-2} (Tg S yr^{-1})$^{-1}$) in this study and previous studies. The sulfate DRF efficiencies are calculated as the response of global DRF to a 20% reduction in local emissions divided by the 20% of sulfur emissions.

Direct radiative forcing (DRF) efficiency						
	EUR	EAS	NAM	SAS	RBU	MDE
Yu et al. (2013)	–9.8~–5.0	–7.6~–3.2	–10.0~–5.0	–10.8~–5.0		
Stjern et al. (2016)	–15.7~–5.6	–12.1~–4.6	–15.5~–4.1	–28.0~–6.3	–8.9~–4.3	–32.4~–10.9
This study	–5.4	–3.8	–4.8	–7.2	–3.9	–9.4
Total (direct + indirect) radiative forcing efficiency						
	EUR	EAS				
Bellouin et al. (2016)	–13.0 (–22.7~–4.4)	–9.5(–13.6~–2.6)				
This study	–12.0	–11.6				

Specific comments:

1.L139-145: the description about parameterizations and approach that were used to calculate the DRF and IRF is not very clear. Please provide more details.
Response:
We have revised the description. Please see the response to comment #3 of major issues.

2.L157: black carbon only occurs in the accumulation mode in MAM3, so the comparison is meaningless.
Response:
We have deleted this sentence.

3.L162: Please show some details about this validation.
Response:
We have added Fig. S1 to compare the sulfate concentration and surface air temperature between the no-tagging and tagging simulations to validate the sulfur tagging technique used in this study.

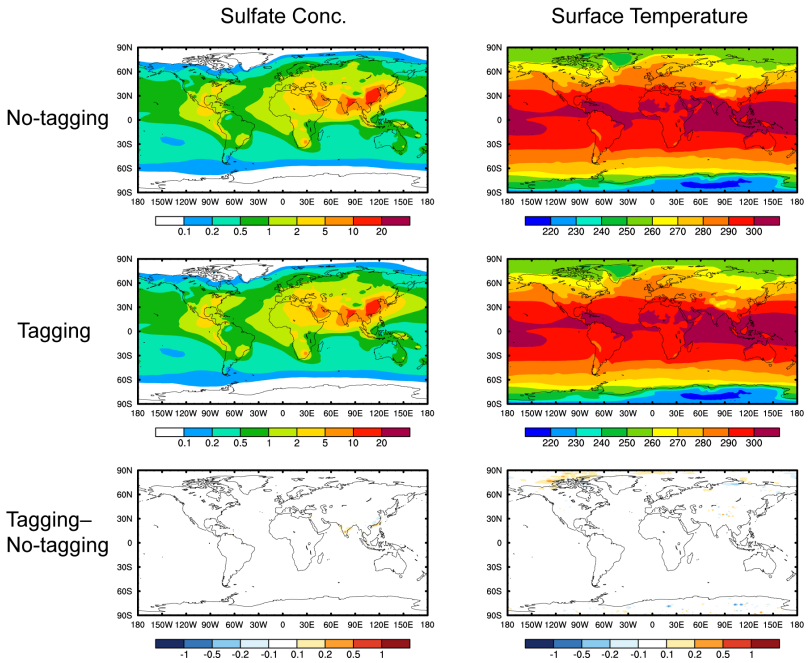

Figure S1. Spatial distribution of annual mean near-surface sulfate concentrations (left, μg m^{-3}) and surface air temperature (right, K) from no-tagging (top), tagging (middle) simulations and their differences (bottom).

4.L198: It is not necessary to show the spatial distributions of SO2 emissions from each tagged region individually. May put Figure 2 into supporting information.
Response:

We have moved this figure to the supporting information as suggested.

5.L203-210: Need some explanations about these seasonal variations.
Response:

We have added some explanations, as "East Asia, RBU and Europe have seasonal peak emissions in boreal winter due to high residential emissions from heating in this season together with higher SO_2 emission from the energy sector. Southern Africa shows larger emission in boreal summer from biomass burning in this season, while emissions from North America are comparable in winter and summer. DMS is emitted over oceans with a boreal winter peak due to phytoplankton blooms over the Southern Ocean."

6.L219: Only North America is used to validate the decomposition of global incremental IRF. Since different regions may have distinct chemical composition and meteorology, and the sensitivity to regional sulfur emissions could vary significantly by region. I think the authors should validate more regions, especially those with large SO2 emissions, e.g., East Asia, Europe and South Asia.
Response:

We agree with the reviewer that using only North America to validate the decomposition of global incremental IRF may not be sufficient. However, it is computationally infeasible to test many of the source regions. Given the large emissions from East Asia, we also performed an additional sensitivity simulation with a 20% reduction in regional sulfur emissions over East Asia and have added the IRF comparison in Fig. S10, with results also now included in the text.

We have also revised the description of the comparison as "The 20% emission from North America results in negative IRF over Eastern U.S. and downwind ocean regions. The 20% emission in East Asia emissions produces negative IRF over the northwestern Pacific. Globally, DMS, North America and East Asia contribute to –0.230 (±0.012), –0.014 (±0.002), and –0.028 (±0.003) W m^{-2}, respectively, of sulfate incremental IRF from the method with sulfur tagging technique, similar to –0.248 (±0.020), –0.018 (±0.019), and –0.028 (±0.018) W m^{-2}, from the individual emission-perturbation simulations."

We have also added a discussion of the noisy spatial distribution of IRF in the emission perturbation method shown in comment #12.

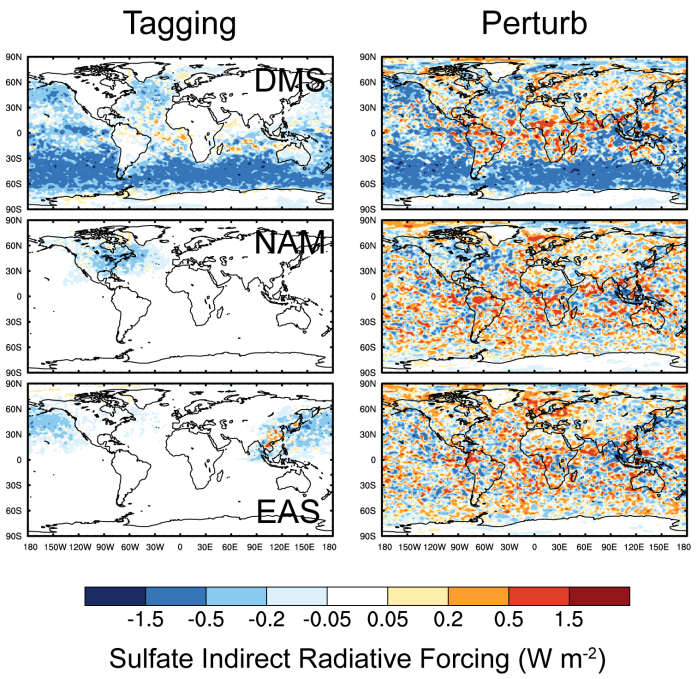

Figure S10. Spatial distribution of annual mean IRF of sulfate (W m^{-2}) induced by a 20% reduction in sulfur emissions from the decomposition using the sulfur tagging method (left panels) and a simple 20% regional/sector emission perturbation (right) for source from DMS (top panels), North America (middle panels), and East Asia (bottom panels).

7.L267: Sulfate has a longer lifetime than black carbon? Need a reference.
Response:
We were thinking about the additional time for the gas-to-particle conversion. It seems to cause some confusion, so we have deleted this sentence.

8.L282-288: If this bias came from the retrieval algorithm, why this overestimation happened more significantly in China than other regions?
Response:
Not only in China, the simulated SO_2 burden is 3 times larger than OMI data over North America, 7 times over Europe, and 5 times over Southeast Asia. We have added these in the manuscript.

9.L294: Here the model results indicated that the export of SO2 from China is under-estimated. However, on Line 291, the authors stated that the inconsistency between simulated results and satellite observations may suggest an overestimation of SO2 at higher altitude. In general, the transport is more efficient in the free troposphere, therefore this indicates a potential overestimation of exporting SO2 from China. Moreover, I would suggest the authors validate total sulfur (SO2+SO4) concentrations and total precipitations over China and downwind region.

Response:

Observational data of SO_2 and sulfate are from different sites and have different time coverage. It is difficult to validate total sulfur over China. Nonetheless, considering that both SO_2 and sulfate are underestimated in the model compared to site observations, the total sulfur is likely to be underestimated. We have added Fig. S5 to validate total precipitation. Over China, CAM5 overestimates precipitation over northern China, which leads to a strong aerosol scavenging and low sulfate concentration over this region. We have added these in the manuscript.

We have also revised the discussion of model-observation comparison for clarification, as "The simulated near-surface SO_2 concentrations, however, are also underestimated by 25% compared to observations over thirteen sites in China (Gong et al., 2014) shown in Fig. S4a, also suggesting a large bias in satellite retrievals or too much SO_2 simulated in higher altitude. In general, the transport is more efficient in the free troposphere. If too much SO_2 is simulated in higher altitude, the near-surface SO_2 concentration is likely to be overestimated over downwind regions. However, the modeled SO_2 concentrations over downwind regions of China are underestimated by 45% compared to observations from EANET sites (Fig. S4b). This indicates that bias in the satellite retrievals may be a significant cause of the inconsistency between modeled and satellite-estimated SO2 burden."

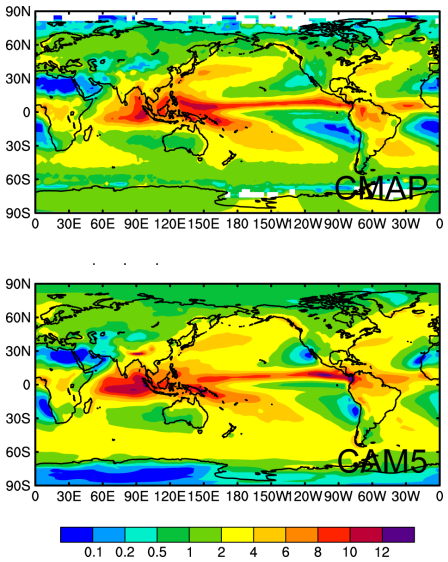

Figure S5. Spatial distribution of annual mean precipitation (mm day^{-1}) from CMAP (Climate Prediction Center's Merged Analysis of Precipitation, top) and simulated in this study (bottom) averaged over 2010–2014.

10.Sections 4 and 5 are too long and need to be shortened. The authors should pay more attention to the major advance (or unique findings) of this study and explain the difference between their results and previous works.

Response:

We have tried our best to shorten the source-receptor description in sections 4 and 5. As we explained in the response to the major comment above, we don't necessarily expect similar results to previous studies. As shown in the newly added Table S9, previous studies only examined influence from limited source regions (2–6). In this study, we have 16 tagged source regions partly owing to the computationally efficient sulfur tagging technique, which extends the source-receptor relationship to the whole globe. For the comparison to limited source regions examined in previous studies, we have discussed the differences and possible biases of the model in response to comment #5 of major issues.

11.L423: In Table S3, why is the concentration efficiency of sulfate over MDE in SON greater than 1?

Response:

The efficiencies over the Middle East show high values in almost all seasons due to dry atmospheric conditions favoring long aerosol lifetime, especially in DJF and

SON. We have emphasized it in the manuscript. The concentration efficiency is calculated as local contribution to the near-surface sulfate concentration divided by local sulfur emission (seasonal emissions multiplied by 4). In SON, The MDE local contribution to concentration is 3.40 μg m^{-3} and its local SO_2 emission is 0.835 Tg S yr^{-1}. Efficiency=3.40/(0.835*4)=1.02 μg m^{-3} (Tg S yr^{-1})$^{-1}$). Since the efficiency is not normalized, it does not have to be less than 1.

12.L522-525: The sensitivity test with a 20% reduction in regional sulfur emissions over North America indicated a large uncertainty associated with this method. Therefore, I would suggest the authors to discuss more on the uncertainties of this calculation.

Response:

Thanks for the suggestion. We have added a discussion of this large uncertainty, as "The latter method has larger noise, seen in both the spatial distributions and large uncertainties (standard deviation) of the incremental IRF. The three emission-perturbed simulations produced similar system noise, with a magnitude of ~0.02 W m^{-2}. The incremental IRF signal is larger than the noise around the source regions whereas noise masks the signal in other regions, leading to large uncertainties. However, in the simulation with all source emissions reduced by 20%, the IRF signal overwhelms noise almost everywhere. With the sulfur tagging technique and decomposition method, the noise is also decomposed into smaller pieces which are, in turn, much smaller than the decomposed incremental IRF signal."

References:

Park, R. J., Jacob, D. J., Field, B. D., Yantosca, R. M., and Chin, M.: Natural and transboundary pollution influences on sulfate-nitrate-ammonium aerosols in the United States: Implications for policy, J. Geophys. Res. Atmos., 109, D15204, doi:10.1029/2003JD004473, 2004.

Chin, M., Diehl, T., Ginoux, P., and Malm, W.: Intercontinental transport of pollution and dust aerosols: implications for regional air quality, Atmos. Chem. Phys., 7, 5501-5517, doi:10.5194/acp-7-5501-2007, 2007.

Hadley, O. L., Ramanathan, V., Carmichael, G. R., Tang, Y., Corrigan, C. E., Roberts, G. C., and Mauger, G. S., Trans-Pacific transport of black carbon and fine aerosol (D<2.5μm) into North America, J. Geophys. Res., 112, D05309, doi:10.1029/2006JD007632, 2007.

Heald, C. L., Jacob, D. J., Park, R. J., Alexander, B., Fairlie, T. D., Yantosca, R. M., and Chu, D. A.: Transpacific transport of Asian anthropogenic aerosols and its impact on surface air quality in the united states, J. Geophys. Res. Atmos., 111, D14310, doi:10.1029/2005JD006847, 2006.

Yu, H., Chin, M., West, J. J., Atherton, C. S., Bellouin, N., Bergmann, D., Bey, I., Bian, H., Diehl, T., Forberth, G., Hess, P., Schulz, M., Shindell, D., Takemura, T., and Tan, Q.: A multimodel assessment of the influence of regional anthropogenic emission reductions on aerosol direct radiative forcing and the role of intercontinental transport, J. Geophys. Res. Atmos., 118, 700-720, doi:10.1029/2012JD018148, 2013.

Bellouin, N., Baker, L., Hodnebrog, Ø., Olivié, D., Cherian, R., Macintosh, C., Samset, B., Esteve, A., Aamaas, B., Quaas, J., and Myhre, G.: Regional and seasonal radiative forcing by perturbations to aerosol and ozone precursor emissions, Atmos. Chem. Phys., 16, 13885-13910, doi:10.5194/acp-16-13885-2016, 2016.

Stjern, C. W., Samset, B. H., Myhre, G., Bian, H., Chin, M., Davila, Y., Dentener, F., Emmons, L., Flemming, J., Haslerud, A. S., Henze, D., Jonson, J. E., Kucsera, T., Lund, M. T., Schulz, M., Sudo, K., Takemura, T., and Tilmes, S.: Global and regional radiative forcing from 20 % reductions in BC, OC and SO4 – an HTAP2 multi-model study, Atmos. Chem. Phys., 16, 13579-13599, doi:10.5194/acp-16-13579-2016, 2016.

Koren, I., Dagan, G., and Altaratz, O.: From aerosol-limited to invigoration of warm convective clouds, Science, 344, 1143–1146, doi:10.1126/science.1252595, 2014.

Liu, J. F., and Mauzerall, D. L.: Potential influence of inter-continental transport of sulfate aerosols on air quality, Environ. Res. Lett., 2, 045029. doi:10.1088/1748-9326/2/4/045029, 2007.

Liu, J., Mauzerall, D. L., and Horowitz, L. W.: Source-receptor relationships between East Asian sulfur dioxide emissions and Northern Hemisphere sulfate concentrations, Atmos. Chem. Phys., 8, 3721–3733, doi:10.5194/acp-8-3721-2008, 2008.

Liu, J. F., Mauzerall, D. L., Horowitz, L. W., Ginoux, P., and Fiore, A. M.: Evaluating inter-continental transport of fine aerosols: 1. Methodology, global aerosol distribution and optical depth, Atmos. Environ., 43, 4327–4338, doi:10.1016/j.atmosenv.2009.03.054, 2009.

Abdul-Razzak, H., and Ghan, S. J.: A parameterization of aerosol activation 2. Multiple aerosol types, J. Geophys. Res., 105, 6837–6844, doi:10.1029/1999JD901161, 2000.

Morrison, H., and Gettelman, A.: A new two-moment bulk stratiform cloud microphysics scheme in the Community Atmosphere Model, version 3 (CAM3). Part I: Description and numerical tests, J. Climate, 21, 3642–3659, doi:10.1175/2008JCLI2105.1, 2008.

Ghan, S. J.: Technical Note: Estimating aerosol effects on cloud radiative forcing, Atmos. Chem. Phys., 13, 9971-9974, doi:10.5194/acp-13-9971-2013, 2013.

Fanourgakis, G., Myriokefalitakis, S., Kanakidou, M., Makkonen, R., Grini, A., Stier, P., Watson-Parris, D., Schutgens, N., Neubauer, D., Lohmann, U., and Nenes, A.,

Evaluation and intercomparison of the aerosol number concentrations and CCNs in global models, in preparation.

McCoy, D. T., Bender, F. A.-M., Mohrmann, J. K. C., Hartmann, D. L., Wood, R., and Grosvenor, D. P.: The global aerosol-cloud first indirect effect estimated using MODIS, MERRA, and AeroCom, J. Geophys. Res. Atmos., 122, 1779–1796, doi:10.1002/ 2016JD026141, 2017.

Zelinka, M. D., Andrews, T., Forster, P. M., and Taylor, K. E.: Quantifying components of aerosol-cloud-radiation interactions in climate models, J. Geophys. Res. Atmos., 119, 7599–7615, doi:10.1002/2014JD021710, 2014.

Manuscript # acp-2017-303

Responses to Reviewer #2

The manuscript by Y. Yang et al. examines the source of sulfate concentration and its direct and indirect radiative effect based on a novel source-receptor analysis technology embedded in CESM. Sources from both anthropogenic and natural emissions are identified for different regions over the globe. The model results comply with the expectation from common knowledge and provide qualitative and comprehensive understanding. This research addresses an important and interesting question of where the sulfate aerosol comes from globally and provides some implication for pollution alleviation. But in terms of scientific significance I would not rank this research in the highest catalog because this method has been used in previous studies (Wang et al., 2013; Yang et al., 2017) with different chemical species and regions. Considering that this research provide large amount of detailed and solid analysis that improves our knowledge on the question, I would like to recommend the publication of this manuscript. Some comments are given below

We thank the referee for all the comments to the manuscript for improving the presentation quality and the recommendation for publication. Regarding the major comment on the relatively low scientific significance, we would argue that the sulfur tagging technique was implemented in the Community Earth System Model (CESM), for the first time, in this study. Our previous studies used a black carbon (BC) tagging method to study the source attributions and impact of BC emitted from different source regions/sectors. The sulfur-tagging and BC-tagging share the same idea, but compared to BC, sulfur has additional gas-phase and aqueous-phase chemical reactions and there are more size-modes to treat sulfate particles. Thus the sulfur-tagging code implementation, testing and validation did take a large amount of additional efforts, and this tool is indeed novel and unique to the present study.

Below, we explain how the comments and suggestions are addressed (our point-by-point responses in blue) and make note of the changes that have been made to the manuscript, attempting to take into account all the comments raised here.

Line 151: Tagging sulfate is “for the first time”, however, not the first time used in CESM. Suggest not emphasizing the novelty.
Response:
Please see our response above. Sulfate tagging is indeed for the first time implemented and used in CESM.

Line 156 to 159: The same reason as above. Suggest just elaborate the method and avoid using phrases such as “In contrast”.

Response:

Thanks for the suggestion. We don’t have to contrast it to BC-tagging, so we changed the description and deleted this phrase.

Line 215: why using 20% reduction to evaluate the indirect effect? Although 20% reduction was used in a previous study (Stjern et al., 2016), this increment of emission is arbitrary to me. Moreover, it hinders comparison with the magnitude of DRF, which compares the forcing with and without 100% aerosols.

Response:

We agree that the 20% reduction of emissions is somewhat arbitrary. However, it follows the AeroCom multi-model experiments design in the framework HTAP (Hemispheric Transport of Air Pollution) to examine the significance of emission reduction. There are numerous studies examined air quality and climate responses to a 20% emission reductions (e.g. Fiore et al., 2009; Fry et al., 2012; Yu et al., 2013; Stjern et al., 2016; Bellouin et al., 2016). We use the same amount of reduction for the purpose of having a fair comparison to these studies. We have added an explanation in the model configuration part, as “The 20% is chosen to follow the experiment design in the framework HTAP2.”

We also agree with the reviewer that the DRF calculated with and without 100% sulfate cannot be directly compared with the incremental IRF induced by the 20% change in emissions. Therefore, we have added in Table S8 the incremental DRF/IRF (calculated from the base and 20% emission reduction simulations) and the standard DRF/IRF (based on the present-day and preindustrial emission simulations), as well as their radiative forcing efficiencies. We have also added a discussion of the comparisons, as “For comparison, Table S8 also includes the incremental DRF calculated with the same simulations for the incremental IRF and the standard anthropogenic DRF between present-day and preindustrial conditions, as well as their efficiencies. The forcing efficiencies are also similar between the incremental and the standard anthropogenic DRF. The IRF and its efficiencies are much higher than those of DRF for sources over or around clean oceanic regions (e.g., DMS, volcanic SO2, emissions from Australia and South America), but much lower for regions with high emissions (e.g., the Middle East, South Asia).”

Table S8. Annual sulfate incremental direct and indirect radiative forcing calculated based on simulations with and without 20% reduction in sulfur emissions globally and standard direct and indirect radiative forcing (W m^{-2}) calculated based on simulations using present-day and preindustrial emissions, as well as the forcing efficiencies (mW m^{-2} (Tg S yr^{-1})$^{-1}$) for all of the sixteen tagged source regions/sectors.

DRF Forcing								
	NAM	CAM	SAM	EUR	NAF	SAF	MDE	SEA
Incremental DRF	-0.003	-0.002	-0.002	-0.004	-0.001	-0.005	-0.006	-0.002
DRF (PD–PI)	-0.015	-0.010	-0.011	-0.018	-0.005	-0.023	-0.031	-0.008
	CAS	SAS	EAS	RBU	PAN	ROW	VOL	DMS
Incremental DRF	-0.001	-0.009	-0.014	-0.002	-0.001	-0.010	-0.007	-0.014
DRF (PD–PI)	-0.006	-0.046	-0.068	-0.011	-0.003	-0.053		
DRF Efficiency								
	NAM	CAM	SAM	EUR	NAF	SAF	MDE	SEA
Incremental DRF efficiency	-4.8	-6.9	-7.1	-5.4	-8.3	-8.4	-9.4	-5.3
DRF efficiency	-4.9	-7.0	-7.1	-5.4	-8.1	-8.5	-9.1	-5.5
	CAS	SAS	EAS	RBU	PAN	ROW	VOL	DMS
Incremental DRF efficiency	-5.4	-7.2	-3.8	-3.9	-5.5	-4.6	-2.7	-4.0
DRF efficiency	-5.2	-7.2	-3.8	-3.9	-5.5	-4.8		
IRF Forcing								
	NAM	CAM	SAM	EUR	NAF	SAF	MDE	SEA
Incremental IRF	-0.014	-0.006	-0.016	-0.004	-0.001	-0.016	-0.001	-0.004
IRF (PD–PI)	-0.082	-0.036	-0.072	-0.032	-0.005	-0.061	0.012	-0.017
	CAS	SAS	EAS	RBU	PAN	ROW	VOL	DMS
Incremental IRF	-0.002	-0.005	-0.028	-0.007	-0.009	-0.042	-0.057	-0.230
IRF (PD–PI)	-0.012	-0.002	-0.117	-0.056	-0.051	-0.202		
IRF Efficiency								
	NAM	CAM	SAM	EUR	NAF	SAF	MDE	SEA
Incremental IRF efficiency	-22.8	-19.8	-50.3	-6.6	-6.2	-28.7	-1.7	-14.1
IRF efficiency	-26.3	-25.0	-44.7	-9.5	-7.9	-22.4	3.5	-11.9
	CAS	SAS	EAS	RBU	PAN	ROW	VOL	DMS
Incremental IRF efficiency	-8.7	-3.7	-7.8	-11.8	-77.3	-18.6	-22.5	-63.2
IRF efficiency	-11.5	-0.3	-6.6	-18.7	-86.6	-18.1		

Line 449: is this 1% difference a coincidence?

Response:

It does not mean '1% difference', but '1750 emission is less than 1% of present-day emission'. We tried to illustrate that DRF of anthropogenic sulfate is calculated here based on present-day and no emission condition ($DRF_{PD} - 0$), while the estimate in IPCC AR5 represents the difference between the present-day and 1750 DRF ($DRF_{PD} - DRF_{1750}$). The global anthropogenic SO_2 emission amount (0.5 Tg/yr) in 1750 is very small, about 0.5% (less than "**1%**") of the 2010–2014 level (109.8 Tg/yr) from the CEDS emission dataset. Therefore, $DRF_{PD} - DRF_{1750} \approx DRF_{PD}$.

References:

Fiore, A. M., et al. (2009), Multimodel estimates of intercontinental source- receptor relationships for ozone pollution, J. Geophys. Res., 114, D04301, doi:10.1029/2008JD010816.

Fry, M. M., et al. (2012), The influence of ozone precursor emissions from four world regions on tropospheric composition and radiative climate forcing, J. Geophys. Res., 117, D07306, doi:10.1029/2011JD017134.

Yu, H., Chin, M., West, J. J., Atherton, C. S., Bellouin, N., Bergmann, D., Bey, I., Bian, H., Diehl, T., Forberth, G., Hess, P., Schulz, M., Shindell, D., Takemura, T., and Tan, Q.: A multimodel assessment of the influence of regional anthropogenic emission reductions on aerosol direct radiative forcing and the role of intercontinental transport, J. Geophys. Res. Atmos., 118, 700-720, doi:10.1029/2012JD018148, 2013.

Stjern, C. W., Samset, B. H., Myhre, G., Bian, H., Chin, M., Davila, Y., Dentener, F., Emmons, L., Flemming, J., Haslerud, A. S., Henze, D., Jonson, J. E., Kucsera, T., Lund, M. T., Schulz, M., Sudo, K., Takemura, T., and Tilmes, S.: Global and regional radiative forcing from 20 % reductions in BC, OC and SO4 – an HTAP2 multi-model study, Atmos. Chem. Phys., 16, 13579-13599, doi:10.5194/acp-16-13579-2016, 2016.

Bellouin, N., Baker, L., Hodnebrog, Ø., Olivié, D., Cherian, R., Macintosh, C., Samset, B., Esteve, A., Aamaas, B., Quaas, J., and Myhre, G.: Regional and seasonal radiative forcing by perturbations to aerosol and ozone precursor emissions, Atmos. Chem. Phys., 16, 13885-13910, doi:10.5194/acp-16-13885-2016, 2016.

Global source attribution of sulfate concentration, direct and indirect radiative forcing

Yang Yang[1*], Hailong Wang[1*], Steven J. Smith[2], Richard Easter[1], Po-Lun Ma[1], Yun Qian[1], Hongbin Yu[3], Can Li[3,4], Philip J. Rasch[1]

[1]Atmospheric Science and Global Change Division, Pacific Northwest National Laboratory, Richland, Washington, USA

[2]Joint Global Change Research Institute, Pacific Northwest National Laboratory, College Park, Maryland, USA

[3]NASA Goddard Space Flight Center, Greenbelt, Maryland, USA

[4]Earth System Science Interdisciplinary Center, University of Maryland, College Park, Maryland, USA

*Correspondence to yang.yang@pnnl.gov and hailong.wang@pnnl.gov

Abstract

The global source-receptor relationships of sulfate concentration, direct and indirect radiative forcing (DRF and IRF) from sixteen regions/sectors for years 2010-2014 are examined in this study through utilizing a sulfur source-tagging capability implemented in the Community Earth System Model (CESM) with winds nudged to reanalysis data. Sulfate concentrations are mostly contributed by local emissions in regions with high emissions, while over regions with relatively low SO_2 emissions, the near-surface sulfate concentrations are primarily attributed to non-local sources from long-range transport. Regional source efficiencies of sulfate concentrations are higher over regions with dry atmospheric conditions and less export, suggesting that lifetime of aerosols, together with regional export, is important in determining regional air quality. The simulated global total sulfate DRF is –0.42 W m^{-2}, with –0.31 W m^{-2} contributed by anthropogenic sulfate and –0.11 W m^{-2} contributed by natural sulfate, relative to a state with no sulfur emissions. In the Southern Hemisphere tropics, dimethyl sulfide (DMS) contributes 17–84% to the total DRF. East Asia has the largest contribution of 20–30% over the Northern Hemisphere mid- and high-latitudes. A 20% perturbation of sulfate and its precursor emissions gives a sulfate incremental IRF of –0.44 W m^{-2}. DMS has the largest contribution, explaining –0.23 W m^{-2} of the global sulfate incremental IRF. Incremental IRF over regions in the Southern Hemisphere with low background aerosols is more sensitive to emission perturbation than those over the polluted Northern Hemisphere.

Deleted: The export of SO_2 and sulfate from Europe contributes 16–20% of near-surface sulfate concentrations over North Africa, Russia/Belarus/Ukraine (RBU) region and Central Asia. Sources from the Middle East account for 15–24% of sulfate over North Africa, Southern Africa and Central Asia in winter and autumn, and 19% over South Asia in spring. Sources in RBU account for 21–42% of sulfate concentrations over Central Asia. East Asia accounts for about 50% of sulfate over Southeast Asia in winter and autumn, 15% over RBU in summer, and 11% over North America in spring. South Asia contributes to 11–24% of sulfate over Southeast Asia in winter and spring.

1. Introduction

Sulfate is an important aerosol that poses health risks (Fajersztajn et al., 2013; Xu et al., 2013; Peplow, 2014) and sulfur deposition is a major driver of ecosystem acidification (Driscoll et al., 2010). Due to long-range transport, local sulfate pollution could result from intercontinental influences, making domestic efforts of improving air quality inefficient (Part et al., 2004; Bergin et al., 2005; Liu and Mauzerall, 2007). In addition, sulfate aerosol substantially perturbs the radiation budget of the Earth directly through scattering incoming solar radiation and indirectly through modifying cloud microphysical properties (Lohmann and Feichter, 2005; Stevens and Feingold, 2009; Myhre et al., 2013). On a global average basis, anthropogenic sulfate aerosol contributes a negative direct radiative forcing (DRF) of -0.4 ± 0.2 W m^{-2} (Boucher et al., 2013). The negative radiative forcing from sulfate partly offsets the positive radiative forcing from greenhouse gases. Therefore, accurate understanding of source attribution of sulfate and its radiative forcing is important for both regional air quality and global climate mitigation (Shindell et al., 2012), which are of great interest to not only science community but also the general public and policymakers.

Sulfate aerosol is produced through oxidation of sulfur dioxide (SO_2) by the hydroxyl radical (OH) in gas phase and aqueous phase oxidation mainly by hydrogen peroxide (H_2O_2) (Martin and Damschen, 1981). The SO_2 precursor is mainly emitted from fossil-fuel combustion (Lu et al., 2010). In recent decades, SO_2 emissions from many developing countries in East Asia and South Asia have increased substantially as a result of accelerated urbanization and rapid economic growth (Streets et al.,

2000; Pham et al., 2005). In contrast, due to air pollution regulations, SO_2 emissions in North America and Europe have decreased significantly since 1980–1990 (Smith et al., 2011; Prechtel et al., 2001). As a consequence, source attribution of sulfate has changed with time over recent decades.

Previous studies have reported that regional aerosols, including sulfate, are produced not only by domestic emissions, but also by distant sources through long-range transport (Jacob et al., 2003; Jaffe et al., 2003; Park et al., 2004; Heald et al., 2006; Liu et al., 2008; Liu et al., 2009; Yu et al., 2012). For example, the strong anthropogenic emissions over East Asia have led to an increasing interest in quantifying the impact of aerosols exported from East Asia. Recent studies indicate that the transpacific transport of sulfate from East Asia contributes to 30–50% of the background (sulfate produced from non-local emissions) surface concentrations in the Western U.S. and 10–30% in the Eastern U.S. (Park et al., 2004; Hadley et al., 2007; Liu et al., 2008), which are larger than contributions from all other foreign sources (Liu et al., 2009). In addition, among the major emitting regions assessed for 2001 conditions, European sources were shown to account for 1–5 μg m^{-3} of surface sulfate concentration over northern Africa and western Asia, and their contribution to East Asia (0.2–0.5 μg m^{-3}) was twice as much as the contribution (0.1–0.2 μg m^{-3}) of Asian sources to North America (Chin et al., 2007).

Due to the important role of sulfate aerosol in the climate system, knowing the relative significance of sulfate radiative forcing from different source regions is useful for climate mitigation. Some previous studies examined the impact of emission

reductions on global and regional DRF and the influence of long-range transport (Yu et al., 2013; Bellouin et al., 2016; Stjern et al., 2016). Yu et al. (2013) examined changes in aerosol DRF resulting from a 20% reduction in anthropogenic emissions from four major polluted regions (namely North America, Europe, East Asia, and South Asia) in Northern Hemisphere, using simulations by nine models from the first phase of the Hemispheric Transport of Air Pollution (HTAP1). They found that 31% of South Asia sulfate aerosol optical depth over South Asia was contributed by non-local sources. Based on the HTAP2, Stjern et al. (2016), using results from ten models, further assessed global and regional DRF from a 20% reduction in emissions over seven regions including North America, Europe, South Asia, East Asia, Russia, the Middle East, and the Arctic. They found that the 20% reduction in emissions in South Asia and East Asia largely perturbed the radiative balance for other regions. However, these studies focused on only the limited number of source regions over the Northern Hemisphere. Continents and subcontinents over the tropics and Southern Hemisphere are also important source and receptor regions for the sulfate radiative forcing, especially for indirect forcing due to stronger aerosol-cloud interactions in clean environments (Koren et al., 2014). Bellouin et al. (2016) quantified the radiative forcing efficiency based on simulations of a 20% reduction in emissions from four source regions/sectors in year 2008, and reported that, with aerosol-cloud interactions included, models simulated higher radiative forcing efficiency of sulfate compared to previous studies (Myhre et al., 2013, Shindell et al., 2013; Yu et al., 2013). Few studies have quantified systematically the global source-receptor

relationships of sulfate indirect radiative forcing that can be attributed to local/non-local source regions and anthropogenic/natural source sectors.

This is the first study that examines source attribution of sulfate radiative forcing with both anthropogenic and natural sources covering the whole globe. In this study, we introduce an explicit sulfur tagging technique into the Community Earth System Model (CESM), in which sulfate aerosol and its precursor emissions from sixteen source regions/sectors (fourteen major source regions and two natural source sectors) are tagged and explicitly tracked. This method allows us to efficiently quantify source region/sector contributions to regional and global sulfate mass concentrations, and direct and indirect radiative forcing (DRF and IRF) of sulfate.

Deleted: We

Model description, emissions datasets, and model experiments are shown in Sect. 2. Section 3 gives the comparison of modeled concentrations of sulfate and SO_2 with a variety of observations. Section 4 shows model results for source attributions of near-surface sulfate and SO_2 concentrations over various receptor regions. Source attributions of DRF and IRF of sulfate are discussed in Section 5. Section 6 summarizes all the results and main conclusions.

2. Methods

2.1. Model description

We use the version 5 of the Community Atmosphere Model (CAM5), which is the atmospheric component of CESM (Hurrell et al., 2013), to simulate the sulfate aerosol and calculate its DRF and IRF. The modal aerosol treatment in CAM5 (Liu et al., 2012)

predicts number mixing ratios and mass mixing ratios of aerosols, distributed in three lognormal modes. A set of modifications to CAM5 that improves wet scavenging of aerosols and convective transport reported by Wang et al. (2013) has also been implemented in the model used in this study. Sulfate is internally mixed with other species in the same aerosol mode and then externally mixed between modes. Sulfate refractive indices at visible wavelengths is 1.43+0.00i. Activation of cloud droplets uses the scheme from Abdul-Razzak and Ghan (2000). The model simulates aerosol-cloud interactions in stratiform clouds using a physically based two-moment parameterization (Morrison and Gettelman, 2008). In addition to the standard radiative fluxes calculated in the model by taking into account all aerosols, the CESM has the capability of diagnosing radiative fluxes in parallel for a subset of aerosol species. The difference between the standard and the diagnosed radiative fluxes can then be attributed to the difference in aerosols considered in the radiation calculations. For example, the difference in shortwave radiation fluxes at the top of the atmosphere (TOA) represents the DRF of the excluded aerosol components in the diagnostic calculation (Ghan, 2013). Using this same method, the DRF of sulfate from any of the sixteen individual tagged regions/sectors can be derived from a pair of diagnostic radiation calculations with and without the particular tagged sulfate considered. To estimate IRF of sulfate from different sources, we define in this study an incremental IRF, calculated as $\Delta(F_{clean} - F_{clear,clean})$, where F is the radiative flux at TOA, F_{clean} is the flux calculated neglecting scattering and absorption by aerosols, $F_{clear,clean}$ is the flux calculated neglecting scattering and absorption by both clouds and aerosols, and

Deleted: The sulfate is internally mixed with other aerosol species in the model. The aerosol optical properties are calculated in the Rapid Radiative Transfer Model (RRTMG, Iacono et al.,2008), with sulfate refractive indices at visible wavelengths of 1.43+0.00i. Activation of cloud droplets uses the scheme from Abdul-Razzak and Ghan (2000). The model simulates aerosol-cloud interactions according to physically based two-moment parameterizations (Morrison and Gettelman, 2008). Parameterizations of aerosol optical properties, cloud droplet nucleation, and aerosol-cloud interactions are described in Neale et al. (2012). In addition to the standard radiative fluxes calculated with all aerosols included, the CESM model has the capability of diagnosing radiative fluxes for a subset of aerosol species. The difference between the standard and the diagnosed shortwave radiative fluxes at the top of the atmosphere (TOA) represents the DRF of the excluded aerosol components in the diagnostic calculation (Ghan, 2013). The DRF of sulfate from individual tagged regions/sectors are calculated with and without individual tagged sulfate from several diagnostics of radiative fluxes (sixteen in this study). To investigate IRF of sulfate from different sources

Δ refers to the differences between the base and emission perturbed simulations. Previous work found that the model did quite well at producing a reasonable sensitivity of number of cloud droplets to sulfate mass concentration, reproducing a significant fraction of the MODIS climatological variability of cloud droplet number concentration (McCoy et al., 2017). Note that, the model only considers aerosol effects on stratiform cloud (Morrison and Gettelman, 2008), and no microphysical impact on convective clouds is included in the present version.

2.2. Sulfur source-tagging

To quantify the regional source attributions of sulfate, for the first time, we implemented in CESM/CAM5 a sulfur source-tagging capability, similar to the black carbon tagging method used in H. Wang et al. (2014) and Yang et al. (2017), through which sulfur gases and sulfate aerosols produced by emissions from independent sources are tagged. The tool can be used to quantify the source attributions of SO_2 and sulfate without perturbing source emissions. The sulfur tagging requires tagging of interstitial and cloud-borne sulfate in each of the three modes as well as SO_2, H_2SO_4 and dimethyl sulfide (DMS) gases. In this study, sulfur species produced by emissions from fourteen geographical source regions and two natural source sectors including volcanic eruptions and DMS from oceans are tagged. The tagged and untagged models have been verified of producing the same SO_2/sulfate properties and meteorology (Fig. S1). While emissions of organic carbon, black carbon, sulfate and its precursor gases are all included in the simulations, the source tagging is used for sulfate and its precursor gases emissions alone.

Deleted: study

Deleted: suggested

Deleted: and can

Deleted: e

Deleted: from satellite

Deleted: The black carbon tagging only required tagging interstitial and cloud-borne black carbon in the accumulation mode. In contrast, t

2.3. Emissions

The CEDS (Community Emissions Data System) anthropogenic emissions (Hoesly et al., 2017) and open biomass burning emissions from Van Marle et al. (2017) that were produced for the CMIP6 model experiments are used in our simulations. In CAM5, 97.5% of SO_2 is emitted directly into the atmosphere and 2.5% is emitted as sulfate aerosol. Natural emissions of volcanic SO_2 and DMS are the same as those used in AeroCom following Neale et al. (2012), which are kept constant throughout the selected years in this study. Figure 1a shows the fourteen geographical source regions tagged in this study, which are consistent with source-receptor regions defined in HTAP2, including North America (NAM), Central America (CAM), South America (SAM), Europe (EUR), North Africa (NAF), Southern Africa (SAF), the Middle East (MDE), Southeast Asia (SEA), Central Asia (CAS), South Asia (SAS), East Asia (EAS), Russia/Belarus/Ukraine (RBU), Pacific/Australia/New Zealand (PAN), and rest of the world (ROW, including oceans and polar continents). Table 1 summarizes emissions of combustion SO_2 (anthropogenic + open biomass burning), volcanic SO_2 emissions (VOL), and DMS emissions over the sixteen tagged source regions/sectors averaged for the most recent five years (2010–2014) and Figure 1b presents relative contributions from individual source regions to the global combustion SO_2 emissions. The global combustion SO_2 emissions rate is 57.6 Tg S yr^{-1}, of which more than 98% come from anthropogenic sources. The combustion SO_2 and sulfate are referred to anthropogenic SO_2 and sulfate hereafter. Detailed information on the anthropogenic emissions of SO_2 can be found in Hoesly et al.

(2017). East Asia, with regional emission of 17.8 Tg S yr^{-1} (31% of global anthropogenic SO_2), has the largest total SO_2 emissions, compared to the other tagged regions. South Asia also emits a large amount of SO_2, 6.4 Tg S yr^{-1} (11%), followed by 3.4 Tg S yr^{-1} (6%) from the Middle East, 3.3 Tg S yr^{-1} (6%) from Europe, 3.1 Tg S yr^{-1} (5%) from North America, and 2.7 Tg S yr^{-1} (5%) from Southern Africa. The other individual tagged regions have weaker emissions, with a combined contribution of less than 5%. However, emissions from ROW contribute 11.2 Tg S yr^{-1} (19%) of SO_2 that are mainly from shipping emissions near the continents. In addition, natural emissions of sulfur are also accounted for, including 12.6 Tg S yr^{-1} of SO_2 from volcanic eruptions, in the range of 10–13 Tg S yr^{-1} derived from the Ozone Monitoring Instrument (OMI) measurement (McLinden et al., 2016), and 18.2 Tg S yr^{-1} of DMS. Figure S2 shows the spatial distribution of SO_2 emissions from each tagged region/sector as well as DMS emissions. Emissions are spatially heterogeneous even within the individual tagged regions. For instance, SO_2 emissions in North America are mainly located in Eastern U.S., and Eastern China accounts for the majority of SO_2 emissions from East Asia. In addition, seasonal variations in emissions are quite different among the source regions (Table 1). East Asia, RBU and Europe have seasonal peak emissions in boreal winter due to high residential emissions from heating in this season together with higher SO_2 emission from the energy sector. Southern Africa shows larger emission in boreal summer from biomass burning in this season, while emissions from North America are comparable in winter and summer due to the bulk of SO_2 emissions arising from baseload electric power generation.

DMS is emitted over oceans with a boreal winter peak due to phytoplankton blooms over the Southern Ocean. These heterogeneous spatial and temporal distributions of emissions could lead to different influences on air quality and radiative forcing over continents and subcontinents near the source regions.

2.4. Model configurations

The CAM5 simulation is conducted using a meteorological nudging method (Ma et al., 2013; Zhang et al., 2014), with winds nudged to the MERRA reanalysis (Rienecker et al., 2011) every 6 hours. Simulations performed are shown below:

1) Base simulation: the simulation is integrated for years 2009–2014, with 2009 for spin-up and 2010–2014 for analysis.
2) All reduction simulation: one sensitivity simulation with the same base model configuration but having a uniform 20% reduction in sulfur (SO_2, sulfate, DMS) emissions globally is performed to quantify source attributions of incremental IRF of sulfate.
3) Source reduction simulations: three sensitivity simulations with the same base model configuration but having a 20% reduction in global DMS emissions and regional sulfur emissions over North America and East Asia, respectively, are performed to validate the decomposition of global incremental IRF into contributions from source regions/sectors using the tagging method.
4) Preindustrial simulation: one sensitivity simulation with the same base model configuration but anthropogenic SO_2 emissions fixed at 1850 level globally is performed to compare incremental IRF and anthropogenic IRF of sulfate.

Deleted: Although volcanic SO_2 emissions are scattered near continents, a large amount of them are injected into the free troposphere.

Deleted: A sensitivity

Deleted: with

Deleted: Two additional sensitivity

Deleted: standard

Deleted: And one additional sensitivity

Deleted: with

The 20% is chosen to follow the experiment design in the framework HTAP2.

All simulations are performed at 1.9° latitude by 2.5° longitude horizontal grids and 30 vertical layers.

3. Model evaluation

To evaluate the model's performance in simulating sulfate with the latest emissions from CEDS inventory, the simulated sulfur concentrations are compared with measurements from regional observation networks. These datasets include the Interagency Monitoring of Protected Visual Environments (IMPROVE), the European Monitoring and Evaluation Programme (EMEP), the East Asian Monitoring Network (EANET), and the China Meteorological Administration Atmosphere Watch Network (CAWNET, Zhang et al., 2012). Sulfate concentrations observed from IMPROVE, EMEP and EANET being used here are from 2010 to 2014, covering the same time period as the simulation, while CAWNET only collected data over 2006–2007. In order to use the CAWNET data to evaluate 2010-2014 simulation results, we decide to scale the observed sulfate mass concentrations using the ratio of CEDS 2010-2014 SO_2 emissions to 2006-2007 emissions over China (which is 0.92) for comparison, thus assuming a linear relationship between SO_2 emissions and sulfate concentrations.

Figure 2 shows the comparison of modeled annual mean near-surface sulfate concentrations with those from the observational networks. The model successfully reproduces the global spatial distribution of sulfate with high concentrations over East Asia and low concentrations over North America and Europe, as well as the spatial

patterns within major continents, for instance, high (low) values over Eastern (Western) U.S. and high (low) sulfate concentrations over Eastern (Western) China. The spatial correlation coefficient between simulated and observed sulfate concentrations globally is +0.86 and is statistically significant at the 95th percentile. Compared to the measurements at the IMPROVE sites over North America, at the EMEP sites over Europe, and at the EANET sites over part of East Asia (only one site in China) and Southeast Asia, the model reproduces sulfate concentrations with biases within ±20%. However, the model largely underestimates the simulated sulfate concentrations in China, with normalized mean biases (NMB) of –54%, compared to the CAWNET observations.

A few factors could be responsible for the bias between the observed and modeled sulfate concentrations. Underestimation of local SO_2 emissions could result in the simulated low sulfate concentrations (Liu et al., 2012; Wang et al., 2013). Too frequent liquid clouds and too strong wet scavenging at the mid- and high latitudes in CESM model can lead to shorter aerosol lifetime and lower concentrations in the simulation (Wang et al., 2011; Liu et al., 2012; Wang et al., 2013). In addition, the underestimation of emissions from upwind regions or strong wet scavenging of aerosols during transport could be another reason for the simulated low bias (Yang et al., 2017). A too low rate of transformation from SO_2 gas to sulfate particles in the model could also contribute to the low bias in sulfate concentrations (Wang et al., 2016; Li et al., 2017). The bias can also result from the fact that the site measurements are point observations, while the model results are grid-cell average

that does not consider subgrid aerosol variations (Qian et al., 2010; R. Wang et al., 2014). In addition, different models show large discrepancies in simulating sulfate over China (Kasoar et al., 2016). The underestimation of sulfate in China can lead to an underestimation of source contribution from East Asia of sulfate concentrations, direct and indirect radiative forcing of sulfate, and forcing efficiencies of sulfate.

To evaluate the model results more broadly, we compare the simulated total column burden of SO_2 with that derived from the OMI measurements (Li et al., 2013), as shown in Fig. S3. Both the model results and the OMI satellite data are averaged over 2010–2014. Compared to the OMI SO_2, the spatial distribution of column burden of SO_2 is reproduced in CAM5, with a statistically significant spatial correlation coefficient of +0.57. However, the model largely overestimates the magnitude of SO_2, especially over China where the simulated values are about 8 times larger than OMI data. Outside of China, simulated SO_2 burdens are 3–7 times larger than OMI data over North America, Europe and Southeast Asia. The large difference between SO_2 burden and OMI retrievals must be due to either an underestimation of SO_2 in OMI products and/or an overestimation of SO_2 burden in the model results. He et al. (2012) compared in situ measurements with OMI SO_2 burden over central China and reported a negative bias of 50% in OMI data, which probably came from cloud contamination, reduced satellite sensitivity to SO_2 due to aerosols, and spatial sampling bias in the satellite data. It is also worth mentioning that satellite column-SO_2 retrievals depend on the vertical distribution of SO_2 assumed in the retrieval algorithm,

Deleted: Considering the longer lifetime of SO_2/sulfate than black carbon, this effect would be expected to be less significant for SO_2/sulfate.

Deleted: Beside

Deleted: the

Deleted: over China

which could be different from either the modeled SO_2 profile in this study or the actual profile, which would introduce a bias.

The simulated near-surface SO_2 concentrations, however, are also underestimated by 25% compared to observations over thirteen sites in China (Gong et al., 2014) shown in Fig. S4a, also suggesting a large bias in satellite retrievals or too much SO_2 simulated in higher altitude. In general, transport is more efficient in the free troposphere. If too much SO_2 is simulated in higher altitude, the near-surface SO_2 concentration is likely to be overestimated over downwind regions. However, the modeled SO_2 concentrations over downwind regions of China are underestimated by 45% compared to observations from EANET sites (Fig. S4b). This indicates that bias in the satellite retrievals may be a significant cause of the inconsistency between modeled and satellite-estimated SO_2 burden.

A less efficient of transformation from SO_2 to sulfate could also lead to underestimation of sulfate. A recent study by Wang et al. (2016) focusing on the sulfate pollution over China and London found that aqueous oxidation of SO_2 by NO_2 was key to an efficient sulfate formation, which has typically been neglected in atmospheric models and is not considered in the CAM5. Another study by Li et al. (2017) found that including an aerosol water ($HRSO_2$) parameterization in SO_2 oxidation in a box model could reproduce the observed rapid sulfate formation in Xi'an over China. More rapid oxidation of SO_2 would reduce SO_2 loss by dry and wet removal and increase sulfate production, which can partly explain the low bias in the simulated sulfate concentrations and high bias in SO_2. In CAM5, 36% of total sulfur

Deleted: SO_2

Deleted: the

Deleted: T

Deleted: ,

Deleted: indicating

Deleted: a

Deleted: can be

Deleted: the reason for

Deleted: e

Deleted: of SO_2 burden

Deleted: the

Deleted:

Deleted: data

Deleted: the transport of SO_2 from China is probably underestimated in the model.

converts into column-integrated sulfate over China, similar to 33% in the Community Multiscale Air Quality (CMAQ) model (He et al., 2012). However, it changes to 21% in the bottom model layer (about 992 hPa), indicating that the oxidation of SO_2 may be underestimated near the surface, which most directly affects the comparison to near-surface observations. This appears to be a plausible explanation for the underestimated sulfate concentrations over China and points to a potentially important direction for future model development.

Biases in simulated precipitation can also lead to biases in sulfate concentrations. Fig. S5 compares annual mean precipitation from CMAP (Climate Prediction Center's Merged Analysis of Precipitation) and that simulated in this study. Over China, CAM5 overestimates precipitation over northern China, which leads to a strong aerosol scavenging and low sulfate concentration over this region.

4. Source attribution of sulfate mass concentrations

Figure 3 shows spatial distributions of modeled fractional contributions to annual near-surface sulfate concentrations. (The absolute concentrations of sulfate are shown in Fig. S6). East Asia, ROW, South Asia and the Middle East contribute 16%, 14%, 10% and 7%, respectively, to global annual mean near-surface sulfate concentration, whereas contributions from the other individual source regions are all less than 5%. Natural emissions of volcanic SO_2 and ocean DMS account for 11% and 16% of global mean sulfate concentrations. Sulfate concentrations are mostly contributed by local sources in regions with high emissions, such as Eastern U.S., Southern Africa, South Asia, and Eastern China, where local source contributions are

larger than 80%. Over regions with relatively low SO_2 emissions, the near-surface sulfate concentrations are primarily attributed to non-local sources from long-range transport. Natural DMS emissions are the source of 80% of near-surface sulfate concentrations over Southern Hemisphere oceans and 20–60% for Northern Hemisphere oceans. Over downwind ocean regions of East Asia, emissions from DMS only account for 20–40% of near-surface sulfate concentrations, showing a stronger influence of regional transport. Sources from volcanic eruption strongly influence sulfate concentrations over eruption regions. They are responsible for 10–40% of near-surface concentrations over Central America and South America, 40–80% over North Africa and Southeast Asia, but only account for about less than 5% over East Asia and South Asia where anthropogenic emissions dominate.

The spatial distribution of sulfate column burden and relative contributions are shown in Figs. S7 and S8, respectively. The global average source attribution of column burden does not differ significantly from that of near-surface concentration. The exception is an increase from 11% to 15% of the relative contribution from VOL to column burden as compared to near-surface concentration due to injection mostly into the free troposphere. The DMS contribution decreases from 16% to 11% to compensate the increase of VOL contribution over oceans. In general, the relative contribution from local source to column burden within a source region is lower than that of near-surface concentration.

Figure 4 presents relative contributions of major sources to near-surface sulfate concentrations in neighboring receptor regions along with seasonal mean wind fields

at 850 hPa. (Table S1 summarizes a complete list of numbers characterizing the source-receptor relationships.) Transport of sulfate shows different patterns in different seasons, due to the seasonal variability in local precursor emissions, lifetime of sulfate, and meteorology, such as wind fields and precipitation.

The export of sulfate from Europe contributes to about 16–20% of near-surface sulfate concentrations over North Africa, RBU and Central Asia in all seasons due to the westerly jet over the eastern European boundary and northerly winds over southern boundary. Sulfate from the Middle East can be effectively transported to the surrounding receptor regions. This export accounts for 15–24% of sulfate concentrations over North Africa, Southern Africa and Central Asia in DJF and SON, and 19% over South Asia in MAM. Sources in the RBU explain about 21–42% of sulfate concentrations over Central Asia, especially in JJA, with northerly winds over north boundary of Central Asia driving transport from this region. Central Asia accounts for 13% of sulfate over the RBU region in DJF when source emissions are the largest. Northerly winds over East Asia in DJF and SON associated with the East Asian winter monsoon transport sulfate from highly polluted Eastern China to Southeast Asia, which accounts for about 50% of near-surface sulfate concentrations over Southeast Asia in these months. The oxidation of SO_2 is expected to peak in JJA because of the high temperature and humidity, and more sunlight. With the help of southerly winds of East Asian summer monsoon, East Asia contributes to 15% of sulfate concentrations over RBU in JJA. Due to the strong westerly jet in MAM, sulfate originating from East Asia has a long-range transport across the North Pacific

Deleted: Sulfate originating from North America, Central America and South America do not show significant contributions (relative contribution less than 10%) to sulfate over other tagged regions in all seasons because of the relatively low sulfate concentrations over these regions and the long intercontinental transport pathways.

Deleted: this region

Deleted: : North Africa, Southern Africa, Central Asia, and South Asia

Deleted: does not have a discernable export of sulfate due to low emissions in most seasons, except that it

Deleted:

and accounts for 11% of near-surface sulfate concentrations and 25% of total imported sulfate (without local contributions) over North America. The transport of sulfate from South Asia contributes 11–24% of sulfate in Southeast Asia in DJF and MAM. These results, however, have additional uncertainties due to the SO_2/sulfate bias in the model for East Asia discussed previously.

Source-receptor relationships for sulfate column burden are summarized in Table S2. Compared to the near-surface concentrations, the sulfate column burden contributed by local sources is much lower in all the receptor regions due to the more efficient long-range transport of aerosols in the free atmosphere. Annually, the local contribution over North America decreases from 67% for near-surface concentration to 33% for column burden. The contributions of non-local sources from East Asia and South Asia increase from 7% and 1% for near-surface concentration to 24% and 10% for column burden, respectively, to the sulfate over North America. In addition, South Asia contribution to sulfate in East Asia, and East Asia contribution to sulfate in RBU and Europe also significantly increase for column burden compared to near-surface concentrations.

Figure 5 shows local contributions (i.e., from sources within the tagged regions) to near-surface sulfate concentrations. Averaged over individual tagged regions, contributions from local sources dominate (i.e., local contributions > 50%) over North America, South America, Europe, Southern Africa, the Middle East, South Asia, and East Asia. Imports dominate near-surface sulfate concentrations (i.e., local contributions < 50%) over the rest of tagged land regions. Within each tagged region,

505 whether local source or import dominates depends on specific locations. For instance,
506 over Eastern China, because of high anthropogenic emissions, local contribution to
507 sulfate concentration is larger than 80%, whereas import from other source regions
508 dominates sulfate over the less economically developed Western China. The same
509 difference can be found between Eastern and Western U.S. of the tagged North
510 America. Over oceans in the Southern Hemisphere, natural sources of DMS
511 contribute the largest to local sulfate concentrations (Fig. 3), whereas long-range
512 transport dominates over the North Pacific in DJF and MAM.
513 Figure 6 presents the aggregate, seasonal relative source contributions to area
514 weighted average near-surface sulfate concentrations over land/ocean in the
515 Northern/Southern Hemisphere. Over land in the Northern Hemisphere, sulfate
516 concentration is mainly attributed to sources from East Asia, South Asia, the Middle
517 East, ROW and volcanic eruption, with relative contributions of 22–29%, 9–16%, 8–
518 14%, 9–11%, and 6–13%, respectively. Over ocean in the Northern Hemisphere,
519 although contribution from ROW, volcanic SO_2 and DMS increase dramatically
520 compared to land, contributions from East Asia and South Asia do not have a large
521 decrease, especially in DJF, MAM and SON when aerosol outflow from Asia is strong
522 (Yu et al., 2012; Yang et al., 2015). Over land in the Southern Hemisphere, mean
523 sulfate concentration is dominated by sources in Southern Africa, having a
524 contribution of 33–43%, followed by 13–25% from South America. Emissions from
525 DMS drive sulfate over ocean in the Southern Hemisphere in all seasons contributing
526 27–63% of sulfate, although Southern Africa contributes 20% of sulfate in JJA.

Figure 7 shows seasonal and annual mean regional concentration efficiencies of sulfate from the tagged source regions/sectors, defined as the local contribution to near-surface sulfate concentration divided by the corresponding sulfur emissions from that region. (Table S3 provides the numeric values.) The regional concentration efficiency represents the relationship between local contribution to sulfate concentration and local emission, which is influenced by many factors, such as local production of sulfate from the emitted SO_2, aerosol removal and export. Note that, the receptor region of ROW is used to calculate efficiencies of the VOL and DMS source sectors, which leads to low biases in efficiencies. The efficiencies over the Middle East show high values in almost all seasons due to dry atmospheric conditions favoring long aerosol lifetime, especially in DJF and SON (e.g., Wang et al., 2014; Stjern et al., 2016). The efficiencies are also high over South Asia in DJF and SON, but low in MAM and JJA due to strong wet removal during the South Asian summer monsoon season. North Africa and Central Asia also show high efficiencies resulted from less precipitation. Although East Asia does not have much precipitation in DJF, the efficiency is low because a large amount of sulfate is transported outside East Asia. It suggests that the lifetime of aerosols, mainly driven by wet deposition, together with regional export, is important in determining the local contribution to near-surface concentrations or regional air quality.

5. Source attribution of direct and indirect radiative forcing of sulfate

548 The modeled global annual mean sulfate total DRF here is –0.42 W m^{-2}, with –
549 0.31 W m^{-2} contributed by anthropogenic sulfate and –0.11 W m^{-2} contributed by
550 natural sulfate (e.g., relative to a state with no natural emissions). The DRF of
551 anthropogenic sulfate is –0.4±0.2 W m^{-2} provided in the Fifth Assessment Report of
552 the Intergovernmental Panel on Climate Change (IPCC, 2013). Note that, the DRF of
553 anthropogenic sulfate calculated here is total anthropogenic sulfate, whereas values
554 from IPCC represent changes in anthropogenic sulfate between 1750 and
555 present-day conditions, although this difference is small since 1750 SO_2 emissions
556 are less than 1% of 2010 emissions. Spatial distributions of sulfate DRF, originating
557 from the individual sixteen sources are shown in Fig. S9. The spatial distributions and
558 global contributions of sulfate DRF are similar to those of sulfate column burden (Fig.
559 S7), except that contribution of DMS to global sulfate DRF (18%) is much larger
560 relative to its global column burden (11%). It is because DMS-produced sulfate
561 burden is mostly located between 30°S–30°N (Fig. S7), where insolation is much
562 stronger than at mid- and high latitudes, leading to stronger DRF over these regions.
563 East Asia is the second largest contributor to global sulfate DRF, contributing 16% of
564 global sulfate DRF, followed by 13% from ROW and 11% from South Asia.
565 Figure 8 shows seasonal and zonal mean DRF of sulfate originating from the
566 tagged regions/sectors and the global total. The meridional distribution of DRF is
567 jointly determined by many factors, e.g. sulfate loading, the insolation, cloud cover,
568 and surface albedo. The total sulfate DRF shows a seasonal pattern that has the
569 maximum DRF over 0°–10°N in DJF and over 30°–40°N in JJA, with values between

–0.9 and –1.3 W m^{-2}. The global and annual average sulfate DRF has a contribution of –0.074 W m^{-2} from DMS, –0.068 W m^{-2} from East Asia, –0.054 W m^{-2} from ROW, –0.047 W m^{-2} from South Asia, –0.035 W m^{-2} from VOL, –0.031 W m^{-2} from the Middle East, –0.023 W m^{-2} from Southern Africa, –0.018 W m^{-2} from Europe, –0.016 W m^{-2} from North America, and a total of –0.057 W m^{-2} from all other regions (Table S4).

Figure 9 shows seasonal fractional contributions to sulfate DRF in different latitudinal bands. Over the Southern Hemisphere tropics (30°S–Equator), mid- (60°S–30°S) and high (90°S–60°S) latitudes, DMS has the largest contribution to sulfate DRF in all seasons, with contribution about 17–84%. Sources from Southern Africa contribute about 11–20% of sulfate DRF over the Southern Hemisphere tropic and mid-latitudes, followed by about 10% from South America and ROW. Sources from East Asia account for 6–19% of sulfate DRF over the Southern Hemisphere high latitudes. In the Northern Hemisphere, influence from DMS becomes much weaker, but still substantial. Over the Northern Hemisphere tropics, East Asia, South Asia, ROW, and DMS exert equal contributions of 10–20%. East Asia has the largest contribution of 20–30% over the Northern Hemisphere mid- and high-latitudes, followed by South Asia and ROW.

Sulfate incremental IRF is estimated by using an additional simulation in which sulfur emissions are reduced by 20% for all regions and sectors. The difference in cloud radiative forcing between the control simulation and this second simulation gives the sulfate incremental IRF of the last 20% of sulfur emissions. Regional incremental IRF contributions are calculated by scaling the total incremental IRF in a grid column

Deleted: Emissions originating from East Asia have the largest zonal mean sulfate DRF in almost all seasons, with a maximum around –0.45 W m^{-2} in JJA because of the higher sulfate loading and the more abundant sunlight in JJA. South Asia also strongly contributes to sulfate DRF, followed by sources from ROW, VOL, RBU, and the Middle East. DMS has the largest contribution over 60°S–0° in DJF due to the stronger insolation over the Southern Hemisphere in winter and more ocean DMS emission over these regions, and its DRF contribution is more widespread. Other tagged source regions have a relatively small contribution to the global total DRF, with a seasonal peak DRF less than –0.10 W m^{-2}.

by regional source contributions to sulfate mass concentration reduction averaged from the surface layer to 850 hPa, which is the approximate altitude of cloud base.

Figure 10 shows regional contributions to sulfate incremental IRF from the tagged source regions/sectors. The sulfate incremental IRF is –0.44 W m^{-2}. The spatial pattern is consistent with that of stratiform clouds since the model only considers aerosol effects on stratiform cloud. The strong negative forcing is mainly over oceans. All source contributions to sulfate incremental IRF from the fourteen tagged source regions are less than –0.04 W m^{-2}, probably due to the polluted conditions over or near land. Particles originating from North America, South America, Southern Africa, and East Asia are also transported to ocean regions, leading to a strong negative forcing there. DMS has the largest contribution, explaining –0.23 W m^{-2} of the global sulfate incremental IRF, because complex cloud adjustments are likely to respond sensitively to small changes in aerosol under clean conditions (Rosenfeld et al., 2014), followed by –0.06 W m^{-2} from volcanic emissions. Note that the regional contribution to incremental IRF is simply calculated by decomposing the total incremental IRF with mass concentrations based on two simulations without and with the reduction in emissions. This assumption could introduce biases considering non-linear relationship between mass concentration and IRF of sulfate.

To evaluate this new method for decomposing incremental IRF into different source regions/sector contributions, the IRF for two regions (North America and East Asia) and one sector (DMS) were calculated in a traditional manner using three additional simulations in which SO_2 emissions from North America, East Asia and

Deleted: one

Deleted: two

DMS emissions were reduced by 20%, respectively. The incremental IRF calculated with the two methods are compared in Fig. S10. Although the incremental IRF outside the source regions obtained from the emission perturbation method is noisy, these two methods show similar negative incremental IRF within and near source regions. The 20% DMS leads to strong negative IRF over oceans. The 20% emission from North America results in negative IRF over Eastern U.S. and downwind ocean regions. The 20% emission in East Asia emissions produces negative IRF over the northwestern Pacific. Globally, DMS, North America and East Asia contribute to –0.230 (±0.012), –0.014 (±0.002), and –0.028 (±0.003) W m^{-2}, respectively, of sulfate incremental IRF from the method with sulfur tagging technique, similar to –0.248 (±0.020), –0.018 (±0.019), and –0.028 (±0.018) W m^{-2}, from the individual emission-perturbation simulations. The latter method has larger noise, seen in both the spatial distributions and large uncertainties (standard deviation) of the incremental IRF. The three emission-perturbed simulations produced similar system noise, with a magnitude of ~0.02 W m^{-2}. The incremental IRF signal is larger than the noise around the source regions whereas noise masks the signal in other regions, leading to large uncertainties. However, in the simulation with all source emissions reduced by 20%, the IRF signal overwhelms noise almost everywhere. With the sulfur tagging technique and decomposition method, the noise is also decomposed into smaller pieces which are, in turn, much smaller than the decomposed incremental IRF signal.

Table S5 summarizes the DRF and incremental IRF of sulfate over land/ocean in the Northern/Southern Hemisphere contributed by the tagged source regions/sectors.

Deleted: of and ssources

Deleted: reduction

Deleted: of

Deleted: reduction

Deleted:

Deleted: and

Deleted: W m^{-2}

Deleted:

Deleted: and

Deleted: W m^{-2}

Deleted: noisy

Deleted: maps

Deleted: with the emission perturbation method are due to system noise

Deleted: ±0.018~±

Deleted: 0

Deleted: signal of

Deleted: overwhelms

Deleted: signal of

Deleted: ing

Deleted: signal of

673 Over the fourteen tagged source regions, the total anthropogenic source region
674 contribution to DRF is –0.54/–0.18 W m^{-2} over land in the Northern/Southern
675 Hemisphere, larger than –0.48/–0.12 W m^{-2} over ocean due to the larger sulfate
676 burden near sources. Anthropogenic source contributions to incremental IRF are
677 larger over ocean, with values of –0.23/–0.13 W m^{-2} compared to –0.08/–0.10 W m^{-2}
678 over land in the Northern/Southern Hemisphere, because clouds are more
679 susceptible to aerosol changes in clean environment and there are more stratiform
680 clouds over ocean. For natural source sectors, their contributions are larger over
681 oceans for both DRF and incremental IRF. Over land in the Northern Hemisphere,
682 DRF is mainly driven by emissions from East Asia, South Asia, and the Middle East,
683 whereas incremental IRF is dominated by emissions from North America, RBU and
684 East Asia. The difference in major contributing regions for DRF vs. incremental IRF
685 may be due to changes in cloud susceptibility when background aerosol
686 concentrations are different. North America and RBU have more relatively clean
687 areas (Alaska, N. Canada, parts of Siberia) than South Asia and East Asia, and
688 clouds in the cleaner areas are more susceptible to the 20% emissions reductions.
689 The non-linearity in DRF is much weaker, so the high emissions from South Asia and
690 East Asia dominate DRF. Over ocean in the Northern Hemisphere, East Asia also
691 contributes the largest to DRF and it is the second largest contributor to incremental
692 IRF of sulfate following DMS. Over land in the Southern Hemisphere, emissions from
693 Southern Africa and South America control DRF, whereas incremental IRF are
694 largely attributed to sources from South America, DMS, and PAN

695 (Pacific/Australia/New Zealand). Over ocean in the Southern Hemisphere, both
696 sulfate DRF and incremental IRF are dominated by DMS emissions.
697 Figure 11 shows the seasonal and annual global DRF and incremental IRF
698 efficiencies of sulfate. (Table S6 gives values.) Global DRF efficiency of a source
699 region is defined as the global DRF of sulfate originating from the source
700 region/sector divided by the total sulfur emissions from that region/sector. The global
701 DRF efficiency treats the whole globe as a receptor region, as opposed to a specific
702 region in the regional concentration efficiency definition, considering that aerosol
703 climatic impacts are on a global scale whereas air quality impacts are more important
704 on a regional scale. As the DRF is more closely related to sulfate burden, global
705 sulfate burden efficiencies are also provided in Table S7. The global DRF efficiency
706 for total sulfur emissions is –4.8 mW m^{-2} (Tg S yr^{-1})$^{-1}$. The Middle East, North Africa,
707 and Southern Africa present high DRF efficiencies, as a result of both long aerosol
708 lifetime and strong tropical insolation. These source regions also have high global
709 burden efficiencies.
710 The global IRF efficiency of a source region is calculated as the global
711 contribution of sulfate incremental IRF divided by the changes (i.e., 20% reduction) in
712 sulfur emissions in that region. Unlike the DRF efficiencies, IRF efficiencies are
713 higher over or near ocean regions, with a global IRF efficiency of –5.0 mW m^{-2} (Tg S
714 yr^{-1})$^{-1}$ for the global total 20% of sulfur emissions. PAN and DMS have the largest IRF
715 efficiencies because PAN has a relatively clean environment compared to other
716 regions and DMS is emitted over clean oceans. Cloud properties are more

susceptible to aerosol perturbations in a more pristine environment. Although the background aerosols in South America are not so low, sulfate originating from this region has a large contribution to sulfate over oceans of the Southern Hemisphere, explaining a large IRF efficiency from that region.

In addition to the incremental IRF and efficiency, we also calculated the anthropogenic sulfate IRF and its efficiency between present-day and preindustrial conditions with an additional simulation, in which anthropogenic SO_2 emissions are fixed at the 1850 level, and compared these values with those from the 20% sulfur emission reduction simulation in Table S8. The modeled annual and global mean anthropogenic sulfate IRF here is -0.74 W m^{-2}, which is comparable to -0.45 ± 0.5 W m^{-2} of IRF for total anthropogenic aerosols from IPCC (2013). The anthropogenic IRF contributed from individual source regions is about 3–6 times larger than the incremental IRF, in agreement with about 5 times more reduction in SO_2 emissions in the preindustrial simulation than in the 20% sulfur emission reduction simulation. The forcing efficiencies are roughly similar between the incremental and the anthropogenic IRF, indicating a nearly linear relationship between SO_2 emission and sulfate IRF, except for the Middle East and South Asia where concentrated dust and its variability may strongly influence cloud properties and therefore sulfate IRF. Figure S11 shows the anthropogenic sulfate IRF efficiencies that are calculated based on anthropogenic IRF from the present-day and preindustrial condition simulations. The values are similar to the incremental IRF efficiencies, further validating the robust results from the decomposed regional IRF with the sulfur tagging technique.

For comparison, Table S8 also includes the incremental DRF calculated with the same simulations for the incremental IRF and the standard anthropogenic DRF between present-day and preindustrial conditions, as well as their efficiencies. The forcing efficiencies are also similar between the incremental and the standard anthropogenic DRF. The IRF and its efficiencies are much higher than those of DRF for sources over or around clean oceanic regions (e.g., DMS, volcanic SO2, emissions from Australia and South America), but much lower for regions with high emissions (e.g., the Middle East, South Asia).

6. Conclusions and discussions

A sulfur tagging technique is implemented in Community Atmosphere Model (CAM) of the Community Earth System Model (CESM) and used in this study to examine source-receptor relationships of sulfate concentrations, DRF and IRF originating from sixteen regions/sectors (North America, Central America, South America, Europe, North Africa, Southern Africa, the Middle East, Southeast Asia, Central Asia, South Asia, East Asia, RBU, PAN, ROW, VOL, and DMS) for 2010–2014. The anthropogenic emissions came from the CEDS inventory developed for the CMIP6.

Near-surface sulfate concentrations are mostly contributed by local emissions in regions with high emissions, such as Eastern U.S., Southern Africa, South Asia, and Eastern China, where local source contributions exceed 80%. Over regions with

760 relatively low SO_2 emissions, the near-surface sulfate concentrations are primarily
761 attributed to non-local sources from long-range transport.
762 The source-receptor relationships have strong seasonal variations. The export of
763 sulfate from Europe contributes to 16–20% of near-surface sulfate concentrations
764 over North Africa, RBU and Central Asia in all seasons. Sulfate from the Middle East
765 is effectively transported to the surrounding receptor regions and accounts for 15–24%
766 of sulfate concentrations over North Africa, Southern Africa and Central Asia in DJF
767 and SON, and 19% over South Asia in MAM. Sources in RBU account for 21–42% of
768 sulfate concentrations over Central Asia, with a peak contribution in JJA. Northerly
769 winds over East Asia in DJF and SON associated with East Asian winter monsoon
770 transport sulfate from highly polluted Eastern China to Southeast Asia, accounting for
771 about 50% of near-surface sulfate concentrations over Southeast Asia. East Asia
772 also contributes 15% to the near-surface sulfate over RBU in JJA and 11% over North
773 America in MAM. The transport of sulfate from South Asia contributes 11–24% of
774 near-surface sulfate over Southeast Asia in DJF and MAM. Regional sulfate
775 concentration efficiencies are higher over regions with dry atmospheric conditions
776 and less export, suggesting that the lifetime of aerosols mainly driven by wet
777 deposition, together with regional export, is important in determining the regional air
778 quality.
779 The simulated global total sulfate DRF is –0.42 W m^{-2}, with –0.31 W m^{-2}
780 contributed by anthropogenic sulfate and –0.11 W m^{-2} contributed by natural sulfate.
781 DMS has the largest contribution to the global sulfate DRF, followed by East Asia,

ROW and South Asia. In the Southern Hemisphere, DMS contributes 17–84% to the seasonal total sulfate DRF. In the Northern Hemisphere tropics, East Asia, South Asia, ROW, and DMS exert similar contributions of 10–20%. East Asia has the largest contribution of 20–30% over the Northern Hemisphere mid- and high-latitudes, followed by South Asia and ROW.

Sulfate incremental IRF is estimated using an additional simulation in which sulfur emissions are reduced by 20%. The difference in cloud radiative forcing between the control simulation and this second simulation gives the sulfate incremental IRF of the last 20% of sulfur emissions, which is –0.44 W m^{-2} globally. DMS has the largest contribution, explaining –0.23 W m^{-2} of the global sulfate incremental IRF, because of the clean marine background conditions, followed by –0.06 W m^{-2} from volcanic emissions. The tagging method, combined with regional decomposition, provides a computationally efficient method of quantifying regional IRF that has a higher signal to noise as compared to regional perturbation simulations.

The Middle East, North Africa, and Southern Africa have high global DRF efficiencies, due to both longer aerosol lifetimes (from low precipitation) and strong insolation. Regions in the Southern Hemisphere with low background aerosols have stronger global IRF efficiencies than those over the polluted Northern Hemisphere, because cloud properties are more susceptible to aerosol perturbations in a more pristine environment.

Note that, although simulated near-surface sulfate concentrations are in agreement with observed values at the IMPROVE sites over North America and at

804 the EANET sites over part of East Asia and Southeast Asia, the model strongly
805 underestimates sulfate concentrations by –54% in China, compared to site
806 observations from the CAWNET network. Comparison of column-integrated SO_2
807 between model simulation and OMI satellite data shows a possible overestimation of
808 SO_2 in the model. The simulated SO_2 near-surface concentrations, however, are
809 underestimated by 25% compared to observations over thirteen sites in China,
810 suggesting a large bias in satellite retrievals or too much SO_2 simulated at higher
811 altitudes. The model SO_2 concentrations over downwind regions of China are
812 underestimated by 45%, indicating that the transport of SO_2 from China is probably
813 underestimated in the model. A less efficient transformation from SO_2 to sulfate could
814 also lead to the underestimation of sulfate in the model. The underestimation of sulfate
815 over China could lead to the underestimation of contributions from East Asia to remote
816 sulfate concentrations, global DRF and incremental IRF, as well as their efficiencies.
817 Table S9 compares the annual sulfate radiative forcing efficiencies simulated in
818 this study to those in previous multi-model studies (Yu et al., 2013; Bellouin et al.,
819 2016; Stjern et al., 2016). As in the previous studies, the DRF efficiency is calculated
820 as the response of global DRF to a 20% reduction in local emissions divided by the
821 20% of sulfur emissions based on two separate simulations rather than 100% of local
822 emissions in a single simulation (Table S6). The efficiencies based on the 20%
823 emission reduction are very similar to those of the 100% emission reduction,
824 indicating a nearly linear relationship between sulfate DRF and emissions. Compared
825 to Yu et al. (2013) and Stjern et al. (2016), the DRF efficiencies in this study are

around the lower bound for all source regions. Another multi-model intercomparison study also reported a lower sulfate DRF simulated in CAM5 compared to other models (Myhre et al., 2013). The difference in DRF efficiencies likely arises from differences in the estimates of aerosol optical properties. With aerosol-cloud interactions included, the total radiative forcing efficiencies in this study are similar to the best estimates provided by Bellouin et al. (2016). The global IRF in CAM5 was also found to be larger than other models in a nine-model intercomparison study, which was attributed to an strong aerosol induced cloud scattering (Zelinka et al., 2014).

Data availability. All the emissions datasets used in this study can be obtained from https://pcmdi.llnl.gov/projects/input4mips. The sulfate datasets are available from http://vista.cira.colostate.edu/IMPROVE/ for IMPROVE sites, http://www.eanet.asia for EANET sites, and http://www.emep.int for EMEP sites. The OMI satellite-derived total column burden of SO_2 can be downloaded from http://disc.sci.gsfc.nasa.gov/Aura/data-holdings/OMI/omso2e_v003.shtml. The CESM model is publically available at http://www.cesm.ucar.edu/models/cesm1.2/. Our model results can be made available through the National Energy Research Scientific Computing Center (NERSC) severs upon request.

Competing interests. The authors declare that they have no conflict of interest.

Acknowledgments. This research was supported by the National Aeronautics and Space Administration's Atmospheric Composition: Modeling and Analysis Program (ACMAP), award NNH15AZ64I. We also acknowledge support from the U.S. Department of Energy (DOE), Office of Science, Biological and Environmental Research. The Pacific Northwest National Laboratory is operated for DOE by Battelle Memorial Institute under contract DE-AC05-76RLO1830. The CESM project was supported by the National Science Foundation and the DOE Office of Science. The National Energy Research Scientific Computing Center (NERSC) provided computational resources.

References

Abdul-Razzak, H., and Ghan, S. J.: A parameterization of aerosol activation 2. Multiple aerosol types, J. Geophys. Res., 105, 6837–6844, doi:10.1029/1999JD901161, 2000.

Bellouin, N., Baker, L., Hodnebrog, Ø., Olivié, D., Cherian, R., Macintosh, C., Samset, B., Esteve, A., Aamaas, B., Quaas, J., and Myhre, G.: Regional and seasonal radiative forcing by perturbations to aerosol and ozone precursor emissions, Atmos. Chem. Phys., 16, 13885-13910, doi:10.5194/acp-16-13885-2016, 2016.

Bergin, M. S., West, J. J., Keatingm, T. J., and Russell, A. G.: Regional atmospheric pollution and transboundary air quality management, Annu. Rev. Environ. Res., 30 1–37, doi:10.1146/annurev.energy.30.050504.144138, 2005.

Boucher, O., Randall, D., Artaxo, P., Bretherton, C., Feingold, G., Forster, P., Kerminen, V.-M., Kondo, Y., Liao, H., Lohmann, U., Rasch, P., Satheesh, S. K., Sherwood, S., Stevens, B., and Zhang, X. Y.: Clouds and Aerosols. In: Climate Change 2013: The Physical Science Basis. Contribution of Working Group I to the Fifth Assessment Report of the Intergovernmental Panel on Climate Change [Stocker, T.F., D. Qin, G.-K. Plattner, M. Tignor, S.K. Allen, J. Boschung, A. Nauels, Y. Xia, V. Bex and P.M. Midgley (eds.)]. Cambridge University Press, Cambridge, United Kingdom and New York, NY, USA, 571–658, doi:10.1017/CBO9781107415324.016, 2013.

880 Chin, M., Diehl, T., Ginoux, P., and Malm, W.: Intercontinental transport of pollution
881 and dust aerosols: implications for regional air quality, Atmos. Chem. Phys., 7,
882 5501-5517, doi:10.5194/acp-7-5501-2007, 2007.
883 Driscoll, C. T., Lawrence, G. B., Bulger, A. J., Butler, T. J., Cronan, C. S., Eagar, C.,
884 Lambert, K. F., Likens, G. E., Stoddard, J. L., and Weathers, K. C.: Acidic
885 deposition in the Northeastern United States: sources and inputs, ecosystem
886 effects, and management strategies, BioScience, 51, 180–198,
887 doi:10.1641/0006-3568(2001)051[0180:ADITNU]2.0.CO;2, 2001.
888 Fajersztajn, L., Veras, M., Barrozo, L. V., and Saldiva, P.: Air pollution: a potentially
889 modifiable risk factor for lung cancer, Nat. Rev. Cancer, 13, 674-678,
890 doi:10.1038/nrc3572, 2013.
891 Ghan, S. J.: Technical Note: Estimating aerosol effects on cloud radiative forcing,
892 Atmos. Chem. Phys., 13, 9971-9974, doi:10.5194/acp-13-9971-2013, 2013.
893 Gong, D.-Y., Wang, W., Qian, Y., Bai, W., Guo, Y., and Mao, R.: Observed holiday
894 aerosol reduction and temperature cooling over East Asia, J. Geophys. Res.
895 Atmos., 119, 6306–6324, doi:10.1002/2014JD021464, 2014.
896 Hadley, O. L., Ramanathan, V., Carmichael, G. R., Tang, Y., Corrigan, C. E., Roberts,
897 G. C., and Mauger, G. S., Trans-Pacific transport of black carbon and fine aerosol
898 (D<2.5μm) into North America, J. Geophys. Res., 112, D05309,
899 doi:10.1029/2006JD007632, 2007.
900 Hatakeyama S., Ikeda, K., Hanaoka, S., Watanabe, I., Arakaki, T., Bandow,
901 Sadanaga, H., Y., Kato, S., Kajii, Y., Zhang, D., Okuyama, K., Ogi, T., Fujimoto,

902 N., Seto, T., Shimizu, A., Sugimoto, N., and Takami, A.: Aerial observations of air
903 masses transported from East Asia to the Western Pacific: vertical structure of
904 polluted air masses, Atmos. Environ, 97, 456–461,
905 doi:10.1016/j.atmosenv.2014.02.040, 2014.
906 He, H., Li, C., Loughner, C. P., Li, Z., Krotkov, N. A., Yang, K., Wang, L., Zheng, Y.,
907 Bao, X., Zhao, G., and Dickerson, R. R.: SO2 over central China?:
908 Measurements, numerical simulations and the tropospheric sulfur budget, J.
909 Geophys. Res., 117, D00K37, doi:10.1029/2011JD016473, 2012.
910 Heald, C. L., Jacob, D. J., Park, R. J., Alexander, B., Fairlie, T. D., Yantosca, R. M.,
911 and Chu, D. A.: Transpacific transport of Asian anthropogenic aerosols and its
912 impact on surface air quality in the united states, J. Geophys. Res. Atmos., 111,
913 D14310, doi:10.1029/2005JD006847, 2006.
914 Hoesly, R. M., Smith, S. J., Feng, L., Klimont, Z., Janssens-Maenhout, G., Pitkanen,
915 T., Seibert, J. J., Vu, L., Andres, R. J., Bolt, R. M., Bond, T. C., Dawidowski, L.,
916 Kholod, N., Kurokawa, J.-I., Li, M., Liu, L., Lu, Z., Moura, M. C. P., O'Rourke, P.
917 R., and Zhang, Q.: Historical (1750–2014) anthropogenic emissions of reactive
918 gases and aerosols from the Community Emission Data System (CEDS), Geosci.
919 Model Dev. Discuss., doi:10.5194/gmd-2017-43, in review, 2017.
920 Hurrell, J. W., Holland, M. M., Gent, P. R., Ghan, S., Kay, J. E., Kushner, P. J.,
921 Lamarque, J. F., Large, W. G., Lawrence, D., Lind- say, K., Lipscomb, W. H.,
922 Long, M. C., Mahowald, N., Marsh, D. R., Neale, R. B., Rasch, P., Vavrus, S.,
923 Vertenstein, M., Bader, D., Collins, W. D., Hack, J. J., Kiehl, J., and Marshall, S.:

The Community Earth System Model A Framework for Collaborative Research, B. Am. Meteorol. Soc., 94, 1339–1360, 2013.

Iacono, M. J., Delamere, J. S., Mlawer, E. J., Shephard, M. W., Clough, S. A., and Collins, W. D.: Radiative forcing by long-lived greenhouse gases: Calculations with the AER radiative transfer models, J. Geophys. Res., 113, D13103, doi:10.1029/2008JD009944, 2008.

IPCC (2013), Climate Change 2013: the Physical Science Basis. Contribution of Working Group I to the Fifth Assessment Report of the Intergovernmental Panel on Climate Change. Cambridge University Press, Cambridge, United Kingdom and New York, NY, USA, p. 1535.

Jacob, D. J., Crawford, J. H., Kleb, M. M., Connors, V. S., Bendura, R. J., Raper, J. L., Sachse, G. W., Gille, J. C., Emmons, L., and Heald, C. L.: Transport and chemical evolution over the Pacific (TRACE-P) aircraft mission: design, execution, and first results, J. Geophys. Res. Atmos., 108, 1–19, doi:10.1029/2002JD003276, 2003.

Jaffe, D., McKendry, I., Anderson, T., and Price, H.: Six 'new' episodes of transpacific transport of air pollutants, Atmos. Environ., 37, 391–404, doi:10.1016/S1352-2310(02)00862-2, 2003.

Kasoar, M., Voulgarakis, A., Lamarque, J.-F., Shindell, D. T., Bellouin, N., Collins, W. J., Faluvegi, G., and Tsigaridis, K.: Regional and global temperature response to anthropogenic SO_2 emissions from China in three climate models, Atmos. Chem. Phys., 16, 9785-9804, doi:10.5194/acp-16-9785-2016, 2016.

946 Koren, I., Dagan, G., and Altaratz, O.: From aerosol-limited to invigoration of warm
947 convective clouds, Science, 344, 1143–1146, doi:10.1126/science.1252595,
948 2014.
949 Li, C., Joiner, J., Krotkov, N. A., and Bhartia, P. K.: A fast and sensitive new satellite
950 SO_2 retrieval algorithm based on principal component analysis: Application to the
951 ozone monitoring instrument, Geophys. Res. Lett., 40, 6314–6318,
952 doi:10.1002/2013GL058134, 2013.
953 Li, G., Bei, N., Cao, J., Huang, R., Wu, J., Feng, T., Wang, Y., Liu, S., Zhang, Q., Tie,
954 X., and Molina, L. T.: A possible pathway for rapid growth of sulfate during haze
955 days in China, Atmos. Chem. Phys., 17, 3301-3316,
956 doi:10.5194/acp-17-3301-2017, 2017.
957 Liu, J. F., and Mauzerall, D. L.: Potential influence of inter-continental transport of
958 sulfate aerosols on air quality, Environ. Res. Lett., 2, 045029. doi:10.1088/1748-
959 9326/2/4/045029, 2007.
960 Liu, J., Mauzerall, D. L., and Horowitz, L. W.: Source-receptor relationships between
961 East Asian sulfur dioxide emissions and Northern Hemisphere sulfate
962 concentrations, Atmos. Chem. Phys., 8, 3721–3733,
963 doi:10.5194/acp-8-3721-2008, 2008.
964 Liu, J. F., Mauzerall, D. L., Horowitz, L. W., Ginoux, P., and Fiore, A. M.: Evaluating
965 inter-continental transport of fine aerosols: 1. Methodology, global aerosol
966 distribution and optical depth, Atmos. Environ., 43, 4327–4338,
967 doi:10.1016/j.atmosenv.2009.03.054, 2009.

968 Liu, X., Easter, R. C., Ghan, S. J., Zaveri, R., Rasch, P., Shi, X., Lamarque, J.-F.,
969 Gettelman, A., Morrison, H., Vitt, F., Conley, A., Park, S., Neale, R., Hannay, C.,
970 Ekman, A. M. L., Hess, P., Mahowald, N., Collins, W., Iacono, M. J., Bretherton,
971 C. S., Flanner, M. G., and Mitchell, D.: Toward a minimal representation of
972 aerosols in climate models: description and evaluation in the Community
973 Atmosphere Model CAM5, Geosci. Model Dev., 5, 709-739,
974 doi:10.5194/gmd-5-709-2012, 2012.
975 Lohmann, U., and Feichter, J.: Global indirect aerosol effects: A review, Atmos. Chem.
976 Phys., 5, 715–737, doi:10.5194/acp-5-715-2005, 2005.
977 Ma, P.-L., Rasch, P. J., Wang, H., Zhang, K., Easter, R. C., Tilmes, S., Fast, J. D., Liu,
978 X., Yoon, J.-H., and Lamarque, J.-F.: The role of circulation features on black
979 carbon transport into the Arctic in the Community Atmosphere Model version 5
980 (CAM5), J. Geophys. Res. Atmos., 118, 4657–4669, doi:10.1002/jgrd.50411,
981 2013.
982 Martin, L. R., and Damschen, D. E.: Aqueous oxidation of sulfur-dioxide by
983 hydrogen-peroxide at low pH, Atmos. Environ., 15, 1615–1621,
984 doi:10.1016/0004-6981(81)90146-3, 1981.
985 McCoy, D. T., Bender, F. A.-M., Mohrmann, J. K. C., Hartmann, D. L., Wood, R., and
986 Grosvenor, D. P.: The global aerosol-cloud first indirect effect estimated using
987 MODIS, MERRA, and AeroCom, J. Geophys. Res. Atmos., 122, 1779–1796,
988 doi:10.1002/ 2016JD026141, 2017.

McLinden, C. A, Fioletov, V. E., Shephard, M., Krotkov, N., Li, C., Martin, R. V., Moran, M. D., and Joiner, J.: Space-based detection of missing sulfur dioxide sources of global air pollution, Nat. Geosci., 9, 496–500, doi:10.1038/ngeo2724, 2016.

Morrison, H., and Gettelman, A.: A new two-moment bulk stratiform cloud microphysics scheme in the Community Atmosphere Model, version 3 (CAM3). Part I: Description and numerical tests, J. Climate, 21, 3642–3659, doi:10.1175/2008JCLI2105.1, 2008.

Myhre, G., Samset, B. H., Schulz, M., Balkanski, Y., Bauer, S., Berntsen, T. K., Bian, H., Bellouin, N., Chin, M., Diehl, T., Easter, R. C., Feichter, J., Ghan, S. J., Hauglustaine, D., Iversen, T., Kinne, S., Kirkevåg, A., Lamarque, J.-F., Lin, G., Liu, X., Lund, M. T., Luo, G., Ma, X., van Noije, T., Penner, J. E., Rasch, P. J., Ruiz, A., Seland, Ø., Skeie, R. B., Stier, P., Takemura, T., Tsigaridis, K., Wang, P., Wang, Z., Xu, L., Yu, H., Yu, F., Yoon, J.-H., Zhang, K., Zhang, H., and Zhou, C.: Radiative forcing of the direct aerosol effect from AeroCom Phase II simulations, Atmos. Chem. Phys., 13, 1853–1877, doi:10.5194/acp-13-1853-2013, 2013.

Neale, R. B., Chen, C.-C., Gettelman, A., Lauritzen, P. H., Park, S., Williamson, D. L., Conley, A. J., Garcia, R., Kinnison, D., Lamarque, J.-F., Marsh, D., Mills, M., Smith, A. K., Tilmes, S., Vitt, F., Morrison, H., Gameron-Smith, P., Collins, W. D., Iacono, M. J., Easter, R. C., Ghan, S. J., Liu, X., Rasch, P. J., and Taylor, M. A.:

1010 Description of the NCAR Community Atmosphere Model (CAM5), NCAR
1011 Technical Note NCAR/TN-486+STR, 275 pp, 2012.
1012 Park, R. J., Jacob, D. J., Field, B. D., Yantosca, R. M., and Chin, M.: Natural and
1013 transboundary pollution influences on sulfate-nitrate-ammonium aerosols in the
1014 United States: Implications for policy, J. Geophys. Res. Atmos., 109, D15204,
1015 doi:10.1029/2003JD004473, 2004.
1016 Peplow, M.: Beijing smog contains witches' brew of microbes, Nature,
1017 doi:10.1038/nature.2014.14640, 2014.
1018 Pham, M., Boucher, O., and Hauglustaine, D.: Changes in atmospheric sulfur
1019 burdens and concentrations and resulting radiative forcings under IPCC SRES
1020 emission scenarios for 1990–2100, J. Geophys. Res. Atmos., 110, D06112,
1021 doi:10.1029/2004JD005125, 2005.
1022 Prechtel, A., Alewell, C., Armbruster, M., Bittersohl, J., Cullen, J. M., Evans, C. D.,
1023 Helliwell, R., Kopacek, J., Marchetto, A., Matzner, E., Meesenburg, H., Moldan, F.,
1024 Moritz, K., Vesely, J., and Wright, R. F.: Response of sulphur dynamics in
1025 European catchments to decreasing sulphate deposition, Hydrol. Earth Sys. Sci.,
1026 5, 311–325, doi:10.5194/hess-5-311-2001, 2001.
1027 Qian, Y., Gustafson Jr., W. I., and Fast, J. D.: An investigation of the sub-grid
1028 variability of trace gases and aerosols for global climate modeling, Atmos. Chem.
1029 Phys., 10, 6917-6946, doi:10.5194/acp-10-6917-2010, 2010.
1030 Rienecker, M. M., Suarez, M. J., Gelaro, R., Todling, R., Bacmeis- ter, J., Liu, R.,
1031 Bosilovich, M. G., Schubert, S. D., Takacs, L., Kim, G-K, Bloom, S., Chen, J.,

1032 Collins, D., Conaty, A., da Silva, A., Gu, W., Joiner, J., Koster, R. D., Lucchesi, R.,
1033 Molod, A., Owens, T., Pawson, S., Pegion, P., Redder, C. R., Reichle, R.,
1034 Robertson, F. R., Ruddick, A. G., Sienkiewicz, M., and Woollen, J.: MERRA:
1035 NASA's Modern-Era Retrospective Analysis for Research and Applications, J.
1036 Climate, 24, 3624–3648, 2011.
1037 Rosenfeld, D., Sherwood, S., Wood, R., and Donner, L.: Climate effects of
1038 aerosol-cloud interactions, Science, 343, 379–380, doi:10.1126/science.1247490,
1039 2014.
1040 Shindell, D. and Faluvegi, G.: Climate response to regional radiative forcing during
1041 the twentieth century, Nat. Geosci., 2, 294–300, doi:10.1038/ngeo473, 2009.
1042 Shindell, D. T., Lamarque, J.-F., Schulz, M., Flanner, M., Jiao, C., Chin, M., Young, P.
1043 J., Lee, Y. H., Rotstayn, L., Mahowald, N., Milly, G., Faluvegi, G., Balkanski, Y.,
1044 Collins, W. J., Conley, A. J., Dalsoren, S., Easter, R., Ghan, S., Horowitz, L., Liu,
1045 X., Myhre, G., Nagashima, T., Naik, V., Rumbold, S. T., Skeie, R., Sudo, K.,
1046 Szopa, S., Takemura, T., Voulgarakis, A., Yoon, J.-H., and Lo, F.: Radiative
1047 forcing in the ACCMIP historical and future climate simulations, Atmos. Chem.
1048 Phys., 13, 2939–2974, doi:10.5194/acp-13-2939-2013, 2013.
1049 Smith, S. J., van Aardenne, J., Klimont, Z., Andres, R. J., Volke, A., and Delgado
1050 Arias, S.: Anthropogenic sulfur dioxide emissions: 1850–2005, Atmos. Chem.
1051 Phys., 11, 1101-1116, doi:10.5194/acp-11-1101-2011, 2011.
1052 Stevens, B. and Feingold, G.: Untangling aerosol effects on clouds and precipitation
1053 in a buffered system, Nature, 461, 607–613, doi:10.1038/nature08281, 2009.

1054 Stjern, C. W., Samset, B. H., Myhre, G., Bian, H., Chin, M., Davila, Y., Dentener, F.,
1055 Emmons, L., Flemming, J., Haslerud, A. S., Henze, D., Jonson, J. E., Kucsera, T.,
1056 Lund, M. T., Schulz, M., Sudo, K., Takemura, T., and Tilmes, S.: Global and
1057 regional radiative forcing from 20 % reductions in BC, OC and SO4 – an HTAP2
1058 multi-model study, Atmos. Chem. Phys., 16, 13579-13599,
1059 doi:10.5194/acp-16-13579-2016, 2016.
1060 Streets, D. G., Tsai, N. Y., Akimoto, H., and Oka, K.: Sulfur dioxide emissions in Asia
1061 in the period 1985–1997, Atmos. Environ., 34, 4413–4424,
1062 doi:10.1016/S1352-2310(00)00187-4, 2000.
1063 van Marle, M. J. E., Kloster, S., Magi, B. I., Marlon, J. R., Daniau, A.-L., Field, R. D.,
1064 Arneth, A., Forrest, M., Hantson, S., Kehrwald, N. M., Knorr, W., Lasslop, G., Li,
1065 F., Mangeon, S., Yue, C., Kaiser, J. W., and van der Werf, G. R.: Historic global
1066 biomass burning emissions based on merging satellite observations with proxies
1067 and fire models (1750–2015), Geosci. Model Dev. Discuss.,
1068 doi:10.5194/gmd-2017-32, in review, 2017.
1069 Wang, G., Zhang, R., Gomez, M. E., Yang, L., Levy Zamora, M., Hu, M., Lin, Y., Peng,
1070 J., Guo, S., Meng, J., Li, J., Cheng, C., Hu, T., Ren, Y., Wang, Y., Gao, J., Cao, J.,
1071 An, Z., Zhou, W., Li, G., Wang, J., Tian, P., Marrero-Ortiz, W., Secrest, J., Du, Z.,
1072 Zheng, J., Shang, D., Zeng, L., Shao, M., Wang, W., Huang, Y., Wang, Y., Zhu,
1073 Y., Li, Y., Hu, J., Pan, B., Cai, L., Cheng, Y., Ji, Y., Zhang, F., Rosenfeld, D., Liss,
1074 P. S., Duce, R. A., Kolb, C. E., and Molina, M. J.: Persistent sulfate formation

from London Fog to Chinese haze, P. Natl. Acad. Sci USA, 113, 13630–13635, doi:10.1073/pnas.1616540113, 2016.

Wang, H., Easter, R. C., Rasch, P. J., Wang, M., Liu, X., Ghan, S. J., Qian, Y., Yoon, J.-H., Ma, P.-L., and Vinoj, V.: Sensitivity of remote aerosol distributions to representation of cloud–aerosol interactions in a global climate model, Geosci. Model Dev., 6, 765-782, doi:10.5194/gmd-6-765-2013, 2013.

Wang, H., Rasch, P. J., Easter, R. C., Singh, B., Zhang, R., Ma, P.-L., Qian, Y., Ghan, S. J., and Beagley, N.: Using an explicit emission tagging method in global modeling of source-receptor relationships for black carbon in the Arctic: Variations, sources, and transport pathways, J. Geophys. Res. Atmos., 119, 12,888–12,909, doi:10.1002/ 2014JD022297, 2014.

Wang, M., Ghan, S., Ovchinnikov, M., Liu, X., Easter, R., Kassianov, E., Qian, Y., and Morrison, H.: Aerosol indirect effects in a multi-scale aerosol-climate model PNNL-MMF, Atmos. Chem. Phys., 11, 5431-5455, doi:10.5194/acp-11-5431-2011, 2011.

Wang, R., Tao, S., Balkanski, Y., Ciais, P., Boucher, O., Liu, J., Piao, S., Shen, H., Vuolo, M. R., and Valari, M.: Exposure to ambient black carbon derived from a unique inventory and high- resolution model, P. Natl. Acad. Sci. USA, 111, 2459–2463, 2014.

Xu, P., Chen, Y. F., and Ye, X. J.: Haze, air pollution, and health in China, Lancet, 382, 2067, doi:10.1016/S0140-6736(13)62693-8, 2013.

Yang, Y., Liao, H., and Lou, S.: Decadal trend and interannual variation of outflow of aerosols from East Asia: Roles of variations in meteorological parameters and emissions, Atmos. Environ., 100, 141-153, doi:10.1016/j.atmosenv.2014.11.004, 2015.

Yang, Y., Wang, H., Smith, S. J., Ma, P.-L., and Rasch, P. J.: Source attribution of black carbon and its direct radiative forcing in China, Atmos. Chem. Phys. Discuss., doi:10.5194/acp-2016-1032, accepted, 2017.

Yu, H., Remer, L., Chin, M., Bian, H., Tan, Q., Yuan, T., and Zhang, Y.: Aerosols from overseas rival domestic emissions over North America, Science, 337, 566–569, doi:10.1126/science.1217576, 2012.

Yu, H., Chin, M., West, J. J., Atherton, C. S., Bellouin, N., Bergmann, D., Bey, I., Bian, H., Diehl, T., Forberth, G., Hess, P., Schulz, M., Shindell, D., Takemura, T., and Tan, Q.: A multimodel assessment of the influence of regional anthropogenic emission reductions on aerosol direct radiative forcing and the role of intercontinental transport, J. Geophys. Res. Atmos., 118, 700-720, doi:10.1029/2012JD018148, 2013.

Zelinka, M. D., Andrews, T., Forster, P. M., and Taylor, K. E.: Quantifying components of aerosol-cloud-radiation interactions in climate models, J. Geophys. Res. Atmos., 119, 7599–7615, doi:10.1002/2014JD021710, 2014.

Zhang, K., Wan, H., Liu, X., Ghan, S. J., Kooperman, G. J., Ma, P.-L., Rasch, P. J., Neubauer, D., and Lohmann, U.: Technical Note: On the use of nudging for

aerosol–climate model intercomparison studies, Atmos. Chem. Phys., 14, 8631-8645, doi:10.5194/acp-14-8631-2014, 2014.

Zhang, X. Y., Wang, Y. Q., Niu, T., Zhang, X. C., Gong, S. L., Zhang, Y. M., and Sun, J. Y.: Atmospheric aerosol compositions in China: spatial/temporal variability, chemical signature, regional haze distribution and comparisons with global aerosols, Atmos. Chem. Phys., 12, 779-799, doi:10.5194/acp-12-779-2012, 2012.

Table 1. Seasonal emissions (units: Tg S season^{-1}) of combustion (anthropogenic + biomass burning) SO_2 and DMS from the sixteen source regions/sectors in December-January-February (DJF), March-April-May (MAM), June-July-August (JJA), and September-October-November (SON) and annual total emissions (ANN).

	NAM	CAM	SAM	EUR	NAF	SAF	MDE	SEA
DJF	8.313E-01	3.458E-01	3.284E-01	1.073E+00	1.519E-01	6.507E-01	8.388E-01	3.537E-01
MAM	7.016E-01	3.659E-01	3.677E-01	8.251E-01	1.529E-01	5.871E-01	8.421E-01	3.731E-01
JJA	8.761E-01	3.731E-01	4.740E-01	6.456E-01	1.534E-01	8.090E-01	8.398E-01	3.516E-01
SON	7.045E-01	3.550E-01	4.357E-01	7.829E-01	1.518E-01	6.641E-01	8.353E-01	3.517E-01
ANN	3.114E+00	1.440E+00	1.606E+00	3.327E+00	6.099E-01	2.711E+00	3.356E+00	1.430E+00
	CAS	SAS	EAS	RBU	PAN	ROW	VOL	DMS
DJF	3.156E-01	1.593E+00	5.043E+00	8.913E-01	1.266E-01	2.836E+00	3.106E+00	5.991E+00
MAM	2.720E-01	1.626E+00	4.406E+00	7.443E-01	1.352E-01	2.775E+00	3.175E+00	4.770E+00
JJA	2.300E-01	1.605E+00	4.084E+00	6.455E-01	1.597E-01	2.739E+00	3.175E+00	3.537E+00
SON	2.619E-01	1.594E+00	4.299E+00	6.940E-01	1.625E-01	2.813E+00	3.141E+00	3.918E+00
ANN	1.080E+00	6.418E+00	1.783E+01	2.975E+00	5.840E-01	1.116E+01	1.260E+01	1.822E+01

Figure Captions

Figure 1. (a) Tagged source regions (NAM: North America, CAM: Central America, SAM: South America, EUR: Europe, NAF: North Africa, SAF: Southern Africa, MDE: the Middle East, SEA: Southeast Asia, CAS: Central Asia, SAS: South Asia, EAS: East Asia, RBU: Russia/Belarus/Ukraine, PAN: Pacific/Australia/New Zealand and ROW: rest of the world) and (b) the respective percentage contributions to global annual mean combustion SO_2 emissions (anthropogenic + biomass burning) from the individual source regions.

Figure 2. Spatial distribution (left panel) and scatter plot (right) between the simulated and observed annual mean near-surface sulfate concentrations (μg m^{-3}) over years 2010–2014. Observations are from IMPROVE (up pointing triangle), EMEP (square), EANET (down pointing triangle) for years 2010–2014, and CAWNET (circle) for years 2006–2007, which are scaled to 2010–2014 based on the ratio of CEDS 2010-2014 SO_2 emissions to 2006-2007 emissions over China (which is 0.92). Solid lines mark the 1:1 ratio and dashed lines mark the 1:2 and 2:1 ratio. Normalized mean bias (NMB) and correlation coefficient (R) between observation and simulation are shown on the right panel. NMB = $100\% \times \sum(M_i - O_i) / \sum O_i$, where M_i and O_i are the modeled and observed values at site i, respectively.

Figure 3. Spatial distribution of relative contributions (%) to annual mean near-surface sulfate concentrations from each of the tagged source regions/sectors.

Relative contributions to global averaged sulfate from individual source regions/sectors is shown at the bottom right of each panel.

Figure 4. Relative contributions of non-local sources to seasonal near-surface sulfate concentrations (left panels) and wind fields over 850 hPa (right panels). Arrows with numbers show contributions (%) of a source region to sulfate over a receptor region. Only relative concentrations larger than 10% are shown.

Figure 5. Relative contributions (%) of local emissions (inside the tagged regions) to near-surface sulfate concentrations. Contributions from natural source sectors are added to ROW here. Contributions less than 50% are shown in cold colors and those larger than 50% are shown in warm colors.

Figure 6. Relative contributions (%) to near-surface sulfate concentrations averaged over land and ocean of the Northern and Southern Hemisphere from emissions in the sixteen tagged source regions/sectors.

Figure 7. Seasonal and annual mean regional concentration efficiency of sulfate (μg m^{-3} (Tg S yr^{-1})$^{-1}$) of the sixteen tagged source regions/sectors. The efficiency is defined as the local contribution to near-surface sulfate concentration divided by the corresponding sulfur emissions from that region (seasonal emissions multiplied by 4). Error bars indicate 1-σ of mean values during years 2010–2014. The receptor region of ROW is used to calculate efficiency of VOL and DMS.

Figure 8. Contributions to zonal mean sulfate direct radiative forcing (W m^{-2}) from emissions of the tagged regions/sectors shown in colors (left Y axis) and from global total emissions shown in black (right Y axis). Only regions with maximum of zonal mean sulfate direct radiative forcing stronger than –0.1 W m^{-2} are shown here.

Figure 9. Relative contributions (%) from emissions in the sixteen tagged regions/sectors to sulfate direct radiative forcing over the Southern Hemisphere high-latitudes (90°S–60°S), Southern Hemisphere mid-latitudes (60°S–30°S), Southern Hemisphere tropics (30°S–Equator), Northern Hemisphere tropics (Equator–30°N), Northern Hemisphere mid-latitudes (30°N –60°N), and Northern Hemisphere high-latitudes (60°N –90°N).

Figure 10. Spatial distribution of responses of annual mean indirect radiative forcing of sulfate (IRF, W m^{-2}) to a 20% reduction in sulfur emissions (standard simulation – simulation with 20% emission reduction). Regional contributions are calculated as a scaled total incremental IRF in each grid cell by the ratio of source contribution to total sulfate mass concentration reduction averaged from the surface layer to 850 hPa. Regional mean contributions to global incremental IRF of sulfate are shown at the bottom right of each panel.

Figure 11. Seasonal and annual mean global sulfate (a) direct and (b) indirect radiative forcing efficiency (mW m^{-2} (Tg S yr^{-1})$^{-1}$) of the sixteen tagged source regions/sectors. The sulfate radiative efficiency is defined as the global sulfate radiative forcing divided by the corresponding scaled annual sulfur emission (seasonal emission multiplied by 4). Error bars indicate 1-σ of mean values during years 2010–2014.

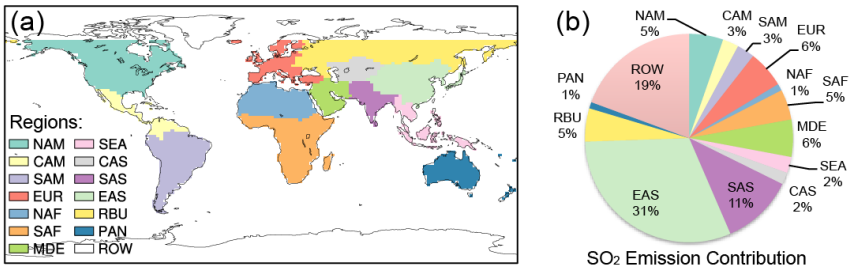

Figure 1. (a) Tagged source regions (NAM: North America, CAM: Central America, SAM: South America, EUR: Europe, NAF: North Africa, SAF: Southern Africa, MDE: the Middle East, SEA: Southeast Asia, CAS: Central Asia, SAS: South Asia, EAS: East Asia, RBU: Russia/Belarus/Ukraine, PAN: Pacific/Australia/New Zealand and ROW: rest of the world) and (b) the respective percentage contributions to global annual mean combustion SO_2 emissions (anthropogenic + biomass burning) from the individual source regions.

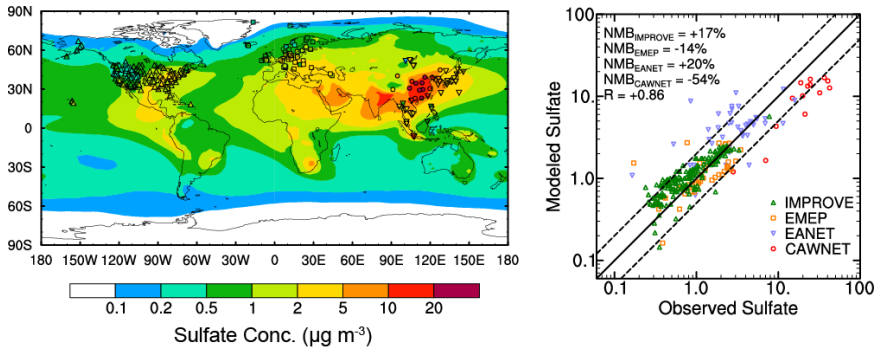

Figure 2. Spatial distribution (left panel) and scatter plot (right) between the simulated and observed annual mean near-surface sulfate concentrations (μg m^{-3}) over years 2010–2014. Observations are from IMPROVE (up pointing triangle), EMEP (square), EANET (down pointing triangle) for years 2010–2014, and CAWNET (circle) for years 2006–2007, which are scaled to 2010–2014 based on the ratio of CEDS 2010-2014 SO_2 emissions to 2006-2007 emissions over China (which is 0.92). Solid lines mark the 1:1 ratio and dashed lines mark the 1:2 and 2:1 ratio. Normalized mean bias (NMB) and correlation coefficient (R) between observation and simulation are shown on the right panel. NMB = $100\% \times \sum(M_i - O_i) / \sum O_i$, where M_i and O_i are the modeled and observed values at site i, respectively.

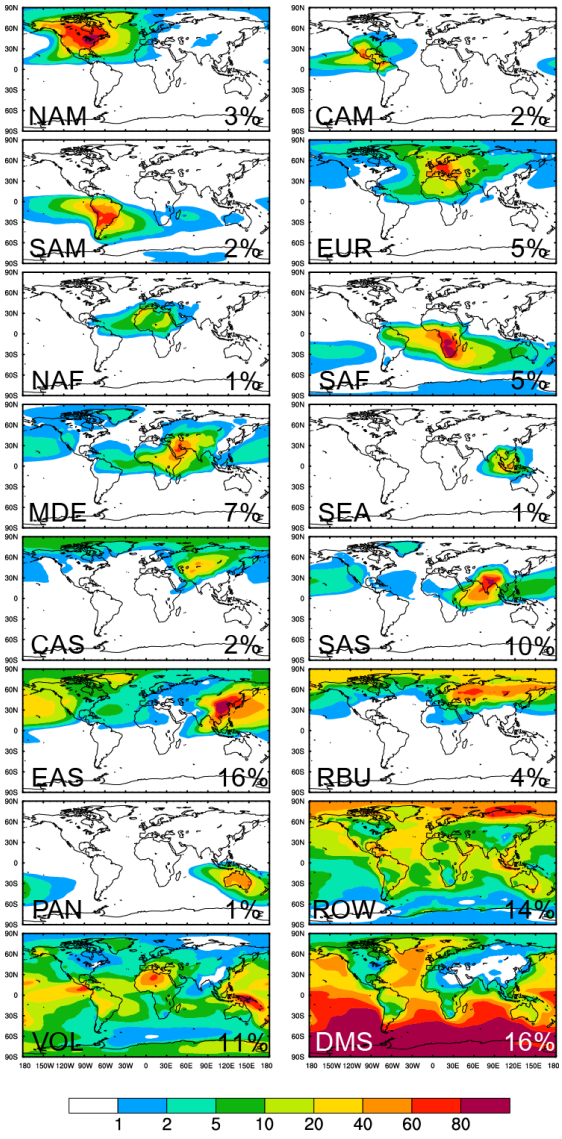

Figure 3. Spatial distribution of relative contributions (%) to annual mean near-surface sulfate concentrations from each of the tagged source regions/sectors. Relative contributions to global averaged sulfate from individual source regions/sectors is shown at the bottom right of each panel.

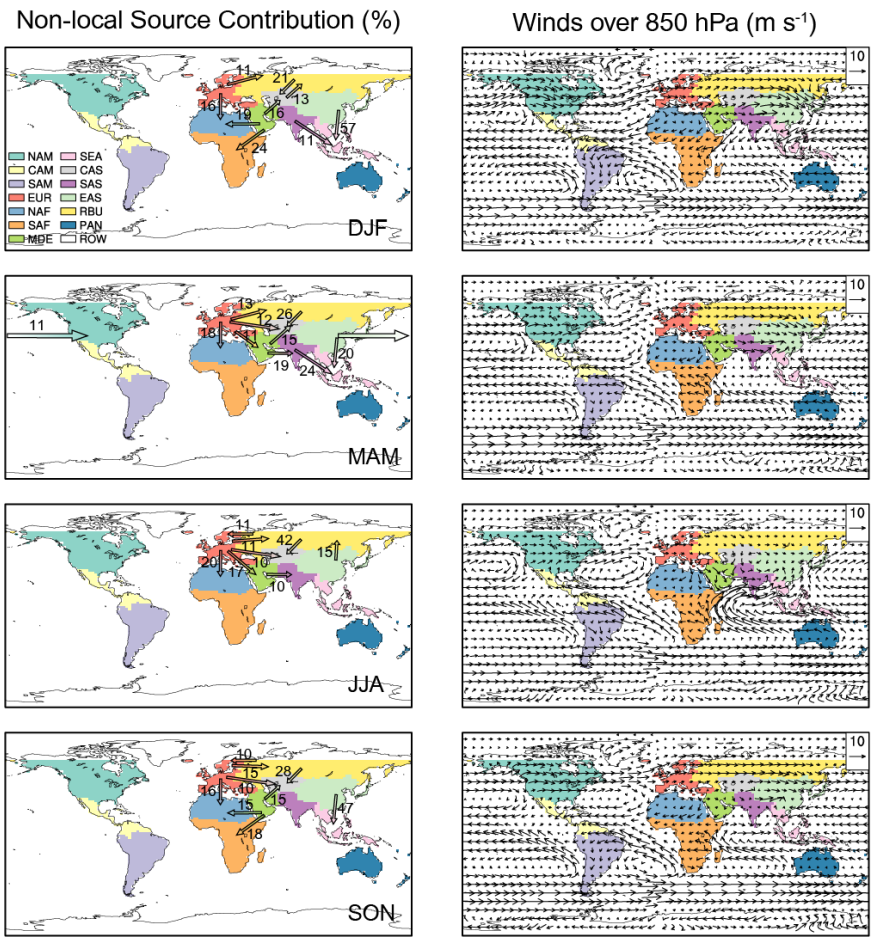

Figure 4. Relative contributions of non-local sources to seasonal near-surface sulfate concentrations (left panels) and wind fields over 850 hPa (right panels). Arrows with numbers show contributions (%) of a source region to sulfate over a receptor region. Only relative concentrations larger than 10% are shown.

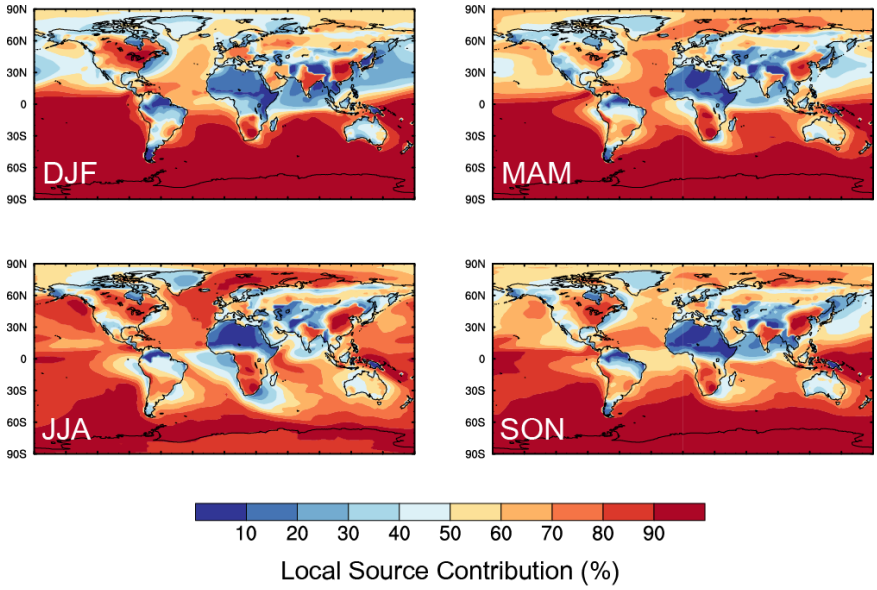

Figure 5. Relative contributions (%) of local emissions (inside the tagged regions) to near-surface sulfate concentrations. Contributions from natural source sectors are added to ROW here. Contributions less than 50% are shown in cold colors and those larger than 50% are shown in warm colors.

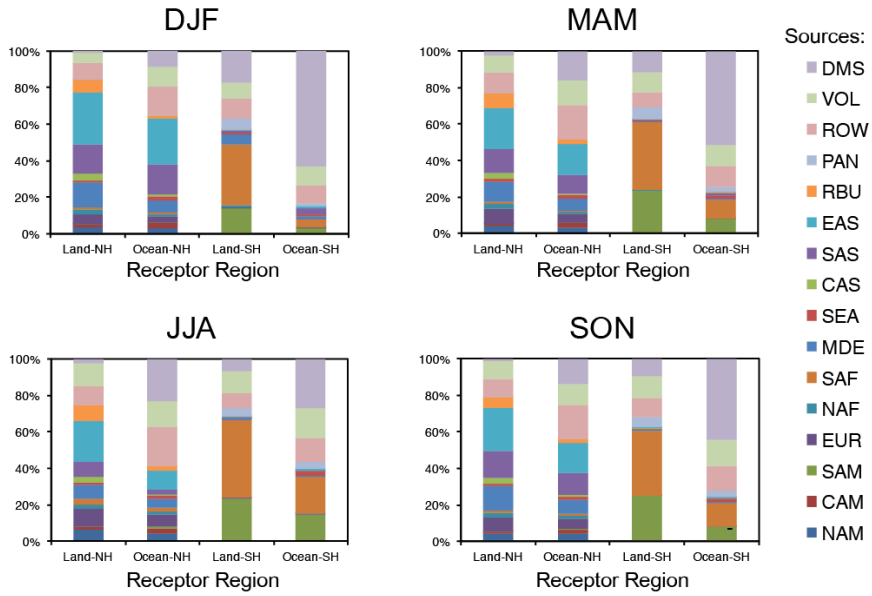

Figure 6. Relative contributions (%) to near-surface sulfate concentrations averaged over land and ocean of the Northern and Southern Hemisphere from emissions in the sixteen tagged source regions/sectors.

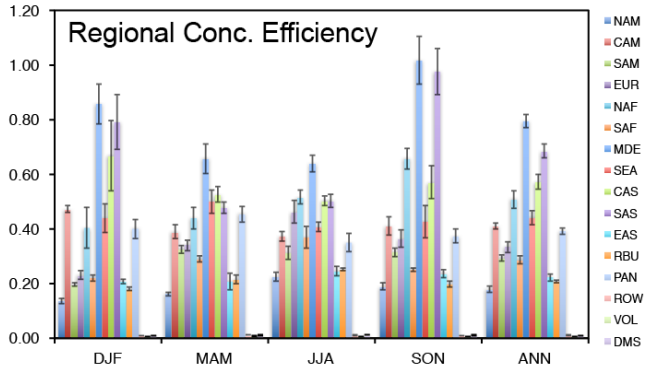

Figure 7. Seasonal and annual mean regional concentration efficiency of sulfate (μg m^{-3} (Tg S yr^{-1})$^{-1}$) of the sixteen tagged source regions/sectors. The efficiency is defined as the local contribution to near-surface sulfate concentration divided by the corresponding sulfur emissions from that region (seasonal emissions multiplied by 4). Error bars indicate 1-σ of mean values during years 2010–2014. The receptor region of ROW is used to calculate efficiency of VOL and DMS.

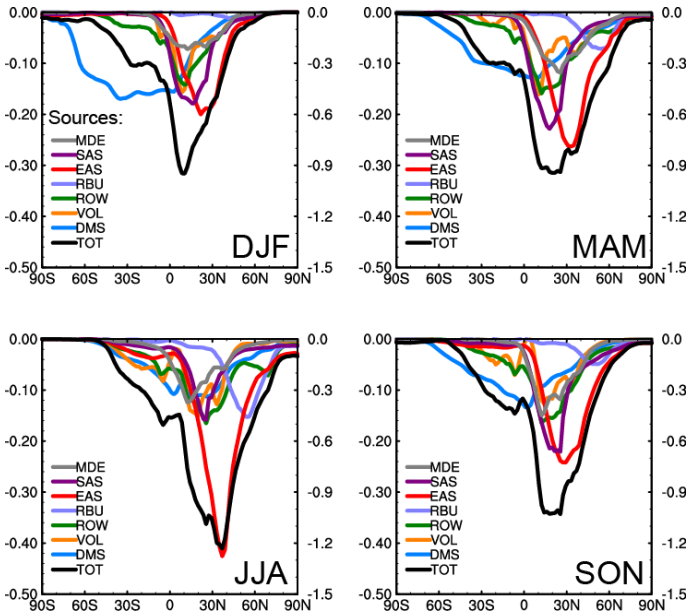

Figure 8. Contributions to zonal mean sulfate direct radiative forcing (W m^{-2}) from emissions of the tagged regions/sectors shown in colors (left Y axis) and from global total emissions shown in black (right Y axis). Only regions with maximum of zonal mean sulfate direct radiative forcing stronger than –0.1 W m^{-2} are shown here.

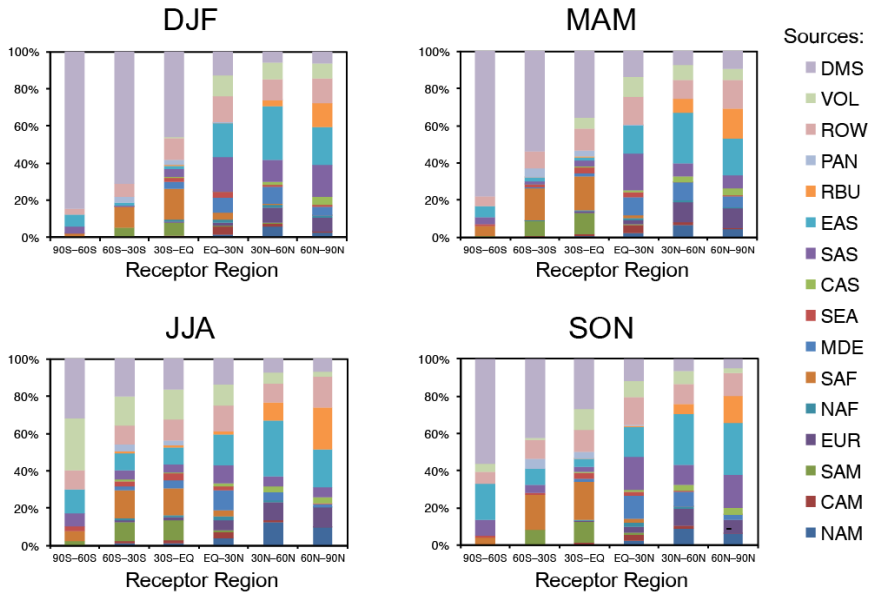

Figure 9. Relative contributions (%) from emissions in the sixteen tagged regions/sectors to sulfate direct radiative forcing over the Southern Hemisphere high-latitudes (90°S–60°S), Southern Hemisphere mid-latitudes (60°S–30°S), Southern Hemisphere tropics (30°S–Equator), Northern Hemisphere tropics (Equator–30°N), Northern Hemisphere mid-latitudes (30°N –60°N), and Northern Hemisphere high-latitudes (60°N –90°N).

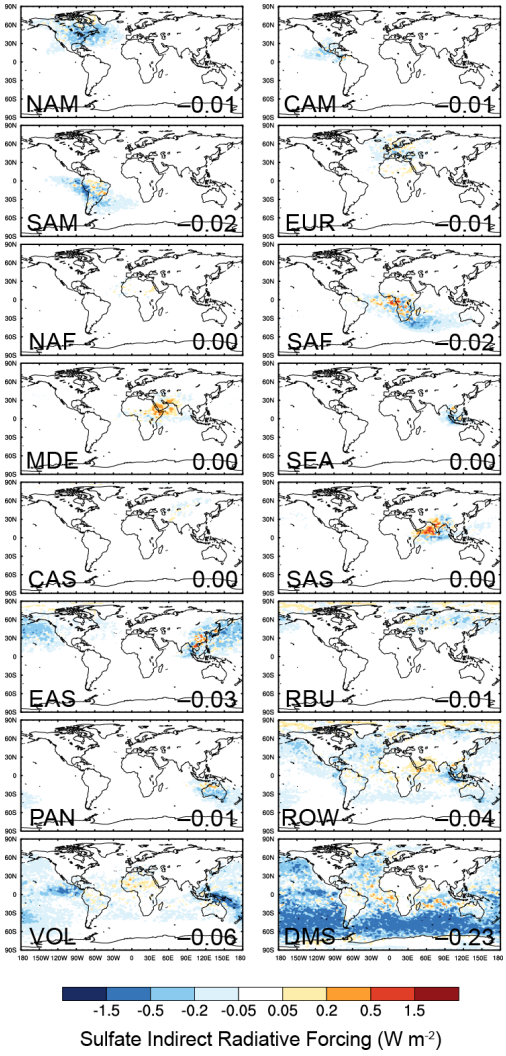

Figure 10. Spatial distribution of responses of annual mean indirect radiative forcing of sulfate (IRF, W m^{-2}) to a 20% reduction in sulfur emissions (standard simulation – simulation with 20% emission reduction). Regional contributions are calculated as a scaled total incremental IRF in each grid cell by the ratio of source contribution to total sulfate mass concentration reduction averaged from the surface layer to 850 hPa. Regional mean contributions to global incremental IRF of sulfate are shown at the bottom right of each panel.

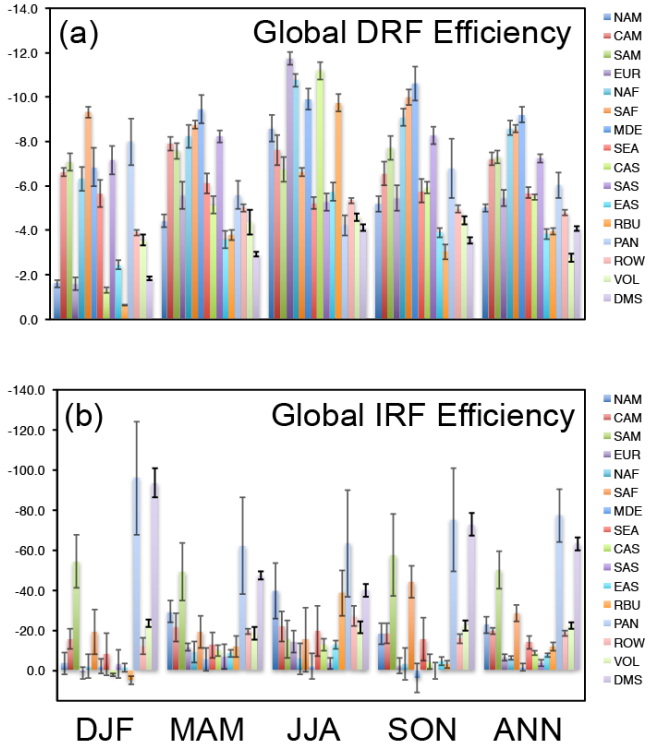

Figure 11. Seasonal and annual mean global sulfate (a) direct and (b) indirect radiative forcing efficiency (mW m^{-2} (Tg S yr^{-1})$^{-1}$) of the sixteen tagged source regions/sectors. The sulfate radiative efficiency is defined as the global sulfate radiative forcing divided by the corresponding scaled annual sulfur emission (seasonal emission multiplied by 4). Error bars indicate 1-σ of mean values during years 2010–2014.